JGR Atmospheres

RESEARCH ARTICLE
10.1029/2018JD029642

Special Section:
Bridging Weather and Climate: Subseasonal-to-Seasonal (S2S) Prediction

The Relation of Intraseasonal Variations With Local Onset and Demise of the Indian Summer Monsoon

Nirupam Karmakar[1] and **Vasubandhu Misra**[1,2,3]

[1]Earth, Ocean and Atmospheric Science Department, Florida State University, Tallahassee, FL, USA, [2]Center for Ocean-Atmospheric Prediction Studies, Florida State University, Tallahassee, FL, USA, [3]Florida Climate Institute, Florida State University, Tallahassee, FL, USA

Abstract Two of the most important hydroclimatic features of the Indian summer monsoon (ISM) rainfall are its onset/demise and intraseasonal oscillations (ISOs) manifested by the active-break cycles. In this study, we aim to understand the quantitative association between these two phenomena. An objective definition of local onset/demise of the ISM based on more than a century-long India Meteorological Department rain gauge observation is taken into consideration. Using multichannel singular spectrum analysis we isolate northward-propagating low-frequency (20–60 days; LF-ISO) and northwestward propagating high-frequency (10–20 days; HF-ISO) ISOs from the daily ISM rainfall. Our results suggest that a large number of local onset (59%) and demise (62%) events occur during positive developing phases and positive decaying phases of two ISOs, respectively, with phase locking between LF-ISO and HF-ISO being particularly important. Local onset is largely associated with favorable phases of ISOs across India except for LF-ISO over eastern India and HF-ISO over western Ghats and central India (CI). We find that local demise is more coherent with the ISO phases, especially with HF-ISO across the domain. We performed a case study to understand large-scale association with the onset of the ISM over CI. In 44 of total 58 cases (1948–2005), when CI onset occurred during favorable LF-ISO or HF-ISO phase, they are either linked with a northward propagation of convection from the equator in LF-ISO time scale (28 cases) or westward propagating structures from the western Pacific in HF-ISO time scale (27 cases).

Key Points:
- Intraseasonal modes of variability account for nearly 60% of local onset and demise events in the Indian summer monsoon (ISM)
- Phase locking between low-frequency and high-frequency ISO modes increases the likelihood of onset/demise of the ISM rainfall
- Propagation of large-scale circulation anomalies associated with both ISOs strongly modulates onset of the ISM over central India

Correspondence to:
N. Karmakar,
nirupam.ju@gmail.com

Citation:
Karmakar N., & Misra, V. (2019). The relation of intraseasonal variations with local onset and demise of the Indian summer monsoon. *Journal of Geophysical Research: Atmospheres*, *124*, 2483–2506. https://doi.org/10.1029/2018JD029642

Received 11 SEP 2018
Accepted 31 JAN 2019
Accepted article online 7 FEB 2019
Published online 5 MAR 2019

Author Contributions
Conceptualization: Nirupam Karmakar, Vasubandhu Misra
Methodology: Nirupam Karmakar
Writing - Original Draft: Nirupam Karmakar
Formal Analysis: Nirupam Karmakar
Investigation: Nirupam Karmakar, Vasubandhu Misra
Supervision: Vasubandhu Misra
Visualization: Nirupam Karmakar
Writing - review & editing: Nirupam Karmakar, Vasubandhu Misra

1. Introduction

The seasonal cycle of the Indian summer monsoon (ISM) is one of the most prominent features of tropical circulation and hydroclimate (Gadgil, 2003). The characterization of the variations of onset and demise of the ISM has been a topic of keen interest of research given its significance to agriculture and the associated economic impact to the entire country (Gadgil & Gadgil, 2006; Giné et al., 2008). Several studies have indicated the variations in the onset of the ISM (Joseph et al., 1994; Misra et al., 2017; Wang & LinHo, 2002). Many of these studies have developed unique indices (usually obtained through area averaging over a critical location) for diagnosing the onset and the demise of the ISM, some of which are exclusively based on rainfall (Ananthakrishnan et al., 1967; Joseph et al., 2006); some others are based on circulation (Syroka & Toumi, 2002; Wang et al., 2009; Webster & Yang, 1992) and land-ocean temperature contrast (Yanai et al., 1992; Zhou & Murtugudde, 2014). Several studies used meridional gradient of tropospheric temperature over the Indian region (Goswami & Xavier, 2005; Sabeerali et al., 2012; Xavier et al., 2007), while others used vertically integrated moisture transport (Fasullo & Webster, 2003) as a proxy to define onset and demise dates of the ISM. Conventionally, India Meteorological Department (IMD) defines onset of the ISM based on rainfall totals over particular stations in Kerala and establishment of strong low-level westerlies in the adjacent region. Climatologically, onset of the ISM over Kerala occurs on 1 June with a standard deviation of 7 days (Pai & Rajeevan, 2009). IMD defines the demise of the ISM by reduction of rainfall and development of a low-level anticyclonic flow over particular regions in India.

The usefulness of single index definitions of onset/demise of the ISM is shown in many aforementioned studies. It is argued that onset of the all-India rainfall (AIR) is strongly related with the changes in large-scale atmospheric and oceanic patterns. However, these definitions do not take into account the local or regional changes in rainfall amount, which may often be linked with synoptic activities. The ISM rainfall exhibits a large heterogeneity across space and time. Climatologically, progression of onset isochrone from southern India to northwestern India occurs over a month (Krishnamurti et al., 2012). This suggests that different

regions experience onset/demise of the ISM at different times. Thus, determination of onset/demise of the ISM could be more useful if it is done locally. Recently, few studies have developed a regional or local definition for onset and demise of the ISM based on rainfall (Misra et al., 2017; Moron & Robertson, 2014). Moron and Robertson (2014) used 1° gridded rainfall data from 1901–2004 and defined onset dates based on "the first significant rains without a potentially crop-threatening dry spell thereafter." They showed that there exist a large spread in the interquartile range of the median of the onset dates from less than 2 weeks over the core monsoon zone to about 30 days over the northwestern regions. Using a 0.25° rainfall data, Moron et al. (2017) recently investigated the potential predictability of the ISM rainfall while analyzing the spatial coherence of interannual variations of subseasonal to seasonal anomalies. They found a drop in this spatial coherence in the core of the monsoon season in contrast to onset and withdrawal phases, hence concluding the subseasonal prediction skill might be higher during the early and the late monsoon phases than during the mature (core) phase of the monsoon season. Misra et al. (2017) defined onset/demise of the ISM using cumulative rainfall anomalies. This definition is adaptive to any given spatial resolution of the rainfall data set and tends to avoid false onset and demise because the definition is anchored to the climatological evolution of the all-India averaged monsoon seasonal cycle.

The movement of the onset isochrone during the month of June over the Indian region is associated with a progressive wetting of the land surface just to the north of isochrone by nonconvective anvil rains (Krishnamurti et al., 2012). This basically helps grow new cloud elements in the north side of the isochrone, and as they develop, they are advected to the north and northwest by upper level divergent flow. Parker et al. (2016) showed that the advancement of the onset isochrones of the ISM also depends upon the intrusion of dry midlevel north westerlies. Therefore, movement of the onset isochrone depends upon several factors and features significant interannual variability. The rapid advancement of the onset of the ISM in 2013 resulted in considerable flooding over the northern state of Uttarakhand (Pai & Bhan, 2014). Whereas, heat wave conditions prevailed over many parts of India in 2014 due to a sluggish advancement of the onset phase (Pai & Bhan, 2015). Moreover, the retreat of the monsoon isochrone is different from a mirror image of the movement of the onset isochrone (Gadgil, 2003). Therefore, there is a need for more accurate prediction of onset/demise isochrones, which largely depends upon how the numerical models capture the behavior of monsoon and its dynamic and thermodynamic characteristics. Sperber and Annamalai (2014) suggested that although the Coupled Model Intercomparison Project-5 models simulate the variability in the date of onset of the ISM quite well, they exhibit delay in the onset of summer rainfall over India. Levine et al. (2013) suggested that this late monsoon onset bias in the Coupled Model Intercomparison Project-5 models often coincides with a particularly large Arabian Sea (AS) cold sea surface temperature (SST) bias during May and June. Chakraborty et al. (2006) suggested that onset of the ISM occurs only after surface moist static energy crosses a threshold value and vertical velocity in the middle troposphere becomes upward. They further suggested from their modeling study that onset of the ISM is significantly delayed by the absence of global orography. Bombardi et al. (2017) examined subseasonal to seasonal retrospective forecasts from three global coupled models and found low prediction skill for the onset and demise of the ISM on subseasonal scales. Therefore, prediction skills for onset/demise of the ISM on subseasonal scale can be improved if we have a better understanding on how subseasonal modes of monsoon rainfall are linked with the onset/demise isochornes.

ISM not only shows a strong seasonal cycle but is also known to exhibit variations across different spatiotemporal scales (Webster et al., 1998). It shows significant intraseasonal variability, and the associated spatiotemporal patterns, driven by the intraseasonal oscillations (ISOs), are considered to be a dominant mode of variability in the ISM rainfall. ISOs significantly modulate the active and break spells of rainfall over India. Two dominant space-time scales are associated with ISO: low-frequency ISO (LF-ISO) exhibiting a periodicity between 3 weeks to 2 months (Gadgil, 2003; Goswami & Ajaya Mohan, 2001; Karmakar et al., 2017b; Krishnamurthy & Shukla, 2007; Lee et al., 2013; Sikka & Gadgil, 1980; Yasunari, 1980), and high-frequency ISO (HF-ISO) showing a variability of roughly 10–20 days (Chen & Chen, 1993; Karmakar et al., 2017b; Krishnamurti & Bhalme, 1976; Krishnamurthy & Shukla, 2007; Murakami, 1976). LF-ISO is characterized by northward propagation of convection from the equatorial Indian Ocean to the foothills of the Himalayas. HF-ISO is often marked by northwestward propagation from the Bay of Bengal (BoB) toward northwestern India. HF-ISO is also associated with a westward-moving equatorial Rossby wave having a wavelength of about approximately 6,000 km (Chatterjee & Goswami, 2004a). Rainfall over central India

(CI) is highly modulated by these ISO modes and phase locking between the two could result into substantial amount of rainfall over the region (Karmakar et al., 2017b; Krishnamurti et al., 1985).

Although onset/demise of monsoon and ISOs are very important features of the ISM, the linkage between the two has not been thoroughly studied, especially considering the local definitions of onset/demise of the ISM. Some of the recent studies on this topic (e.g., Wang et al., 2009; Zhou & Murtugudde, 2014) have used the single, large-scale indices of onset/demise of the ISM to investigate their modulation by LF-ISO. For example, Wang et al. (2009) used a lower atmosphere zonal wind index over the southeast AS to find that westward extension of the convection from eastern equatorial Indian Ocean serves as a robust precursor to the ISM onset over Kerala. They further suggested that the ISM onset is lead by the northeastward progression of ISO from the western equatorial Indian Ocean. More recently, Zhou and Murtugudde (2014) using the mean meridional temperature gradient to measure the land-ocean contrast as an index for the onset of the ISM suggested that a significant fraction of early onset of the ISM is caused by the northward-propagating ISO. But their study also shows that a significant fraction of years have onset of ISM without the influence of ISO. Importantly, the influence of northwestward propagating HF-ISO on onset/demise of the ISM is not investigated in any of the previous studies.

The objective of this study is to assess the degree of influence of ISOs on the variations and evolution of the local onset and demise of the ISM in a quantitative sense. In other words, using rainfall data, we aim to show quantitatively how the local onset/demise events are modulated by the phases of LF-ISO and HF-ISO. Is local ons et always associated with northward-propagating LF-ISO? Or can they be triggered by westward propagating low-pressure structures associated with HF-ISO? The analysis presented in the study not only advances our understanding of the monsoon system but also provides direction toward a diagnostic tool to make probabilistic estimation of onset and demise of the ISM using phase information of ISOs. The paper is organized as the following: Section 2 provides a description about the data sets used in this study and the methodology adopted. Section 3 describes the results, and section 4 provides a short discussion on the results followed by conclusions drawn from this study.

2. Data Set and Methodology

We use IMD 0.25° × 0.25° gridded rainfall data from 1902–2005 (Pai et al., 2014). This data set was constructed using quality controlled data from 6,955 rain gauge stations in India. The data set can be purchased from IMD (http://imdpune.gov.in/ndc_new/Request.html). Misra et al. (2017) used the similar data set to define local onset and demise dates of the ISM. Rainfall over the extreme northern portion (north of 34° N and parts of the states of Himachal Pradesh and Uttarakhand over the foothills of the Himalayas) of India may be highly influenced by orography (Bhatt & Nakamura, 2005), which can lead to complexities with diagnosis of ISO or local onset/demise of the ISM. Moreover number of rain gauge stations used to generate data over these regions are comparatively less (Pai et al., 2014). Therefore, we do not consider data over these regions in any of our analysis. Many earlier studies also neglected these regions to study monsoon variability (Karmakar et al., 2015; Krishnamurthy & Shukla, 2007). We also use National Centers for Environmental Prediction/National Center for Atmospheric Research Reanalysis-1 (Kalnay et al., 1996) data sets to understand large-scale atmospheric patterns during onset/demise of the ISM. These data are provided by the National Oceanic and Atmospheric Administration/Oceanic and Atmospheric Research/Earth System Research Laboratory's Physical Sciences Division (NOAA/OAR/ESRL PSD), Boulder, Colorado, USA, from their website at https://www.esrl.noaa.gov/psd/. These data sets are of 2.5° × 2.5° resolution and is provided from 1948 to the present time. However, since our analysis period is upto 2005, we restrict the usage of this data up to that time period.

2.1. Defining the Local Onset and Demise Dates

Following Noska and Misra (2016), we define daily cumulative anomaly of AIR and marked the onset on the ISM as the first day after the minimum in the daily cumulative anomaly is achieved. The day after the maximum in the daily cumulative anomaly curve marks the demise of the ISM. Daily cumulative anomaly $Cm'(i)$ of AIR for day i and year m is obtained by using the following equation:

$$C'_m(i) = \sum_{n=1}^{i} [D_m(n) - \overline{\overline{C}}], \tag{1}$$

where

$$\overline{\overline{C}} = \frac{1}{MN}\sum_{m=1}^{M}\sum_{n=1}^{N} D_m(n), \tag{2}$$

$D_m(n)$ is the daily AIR for day n and year m, and $\overline{\overline{C}}$ represents the climatology of the annual mean of AIR over N (=365 or 366) days for M years. This approach is based on a method proposed by Liebmann and Marengo (2001) and was also used in Bombardi et al. (2017) to determine onset and demise of the monsoon rainfall over different regions. This simple one parameter definition of onset/demise of the ISM posses many merits and has been verified with the seasonal evolution of other dynamic and thermodynamic variables associated with the ISM for consistency (Noska & Misra, 2016).

We define local onset and demise dates as they are developed in Misra et al. (2017). While we refer to their study for the detailed description, we present here a broad overview of the methodology. Basically, the climatological onset and demise of the ISM over every grid point is defined using the daily cumulative rainfall anomaly derived from corresponding daily rainfall climatology. This is similar to how it is done for the daily AIR as described earlier. In the next step, climatological onset/demise of AIR is defined by using daily cumulative anomaly of the daily climatological AIR. Local onset and demise of the ISM for every year is calculated using the minimum and maximum values in the daily cumulative anomaly curve of the year in the immediate vicinity of its climatological departure from onset and demise, respectively. The neighborhood within which the minimum and maximum values are sought out is estimated using the difference between climatological local and AIR onset/demise is then calculated at each grid point. This essentially is used to average out the transients. Anchoring the local onset and demise to the AIR onset and demise thus significantly reduces the possibility of detecting false onset or demise, which could be attributed to some local processes or scattered small-scale events not associated with the large-scale evolution of the ISM.

2.2. Extraction of ISO Modes

The extraction of ISO modes in the rainfall data is done using multichannel singular spectral analysis (MSSA; Ghil et al., 2002; Plaut & Vautard, 1994). This data-adaptive filtering technique is quite successful in extracting oscillatory signals from a short and noisy time series and has been used in many studies recently to understand the behavior of Indian monsoon (Karmakar et al., 2017a, 2017b; Karmakar & Krishnamurti, 2018; Krishnamurthy & Shukla, 2007; Moron et al., 2012). We removed the daily climatology at each grid point from the 104-year daily data. Daily climatology is defined as the mean on each calendar day over the 104-year-long period. Then a prefiltering is applied with a 5-day moving mean to remove very high-frequency fluctuations. Each year's data are then fed into the MSSA algorithm, which determines the oscillatory modes present in the data.

MSSA has become a very popular technique in recent years to analyze spatiotemporal behavior of short and noisy time series. MSSA is advantageous compared to many other harmonic analyses or fast Fourier analysis, primarily because the shape and bandwidth of the filters in MSSA are functions of the data provided by the user. This technique is tailored to capture anharmonic oscillations arising from nonlinear phenomena in the system. In MSSA, lagged copies of the data are augmented to construct a lag-covariance matrix, which is diagonalized to obtain space-time empirical orthogonal functions and temporal principal components. An oscillation is detected in the data if the phase of two space-time empirical orthogonal functions are in quadrature and the associated eigenvalues are nearly equal (Plaut & Vautard, 1994). We used a window length of 60 days, which is sufficient enough to resolve oscillations in the intraseasonal time period using year-long data (Plaut & Vautard, 1994). Further, a statistical test with 1,000 red-noise surrogates is used to avoid the possibility of any random fluctuation and noise being treated as an oscillatory mode (Allen & Robertson, 1996). Significant oscillatory modes that capture oscillations with a periodicity of 20–60 days are used to reconstruct LF-ISO modes. The reconstruction is defined as LF-ISO for each year. Similarly, HF-ISO is extracted by retaining modes that have periodicity of 10–20 days. LF-ISO and HF-ISO are of the same dimension as of the actual input data. HF-ISO explains on average 22.4% of the variability of the daily rainfall anomaly (5-day smoothed) each year with a standard deviation of 5.7%. Similarly, variance explained by LF-ISO has a mean of 30.2% during 1902–2005 with a standard deviation of 7.0%. Similar approach was adopted in Karmakar et al. (2017b) and intrinsic features of LF-ISO and HF-ISO over the Indian domain using satellite-derived rainfall product were shown. We refer to Ghil et al. (2002) for more details about the technique and Karmakar et al. (2017b) for how MSSA is used in the ISM rainfall context and further methodological details to extract ISO modes.

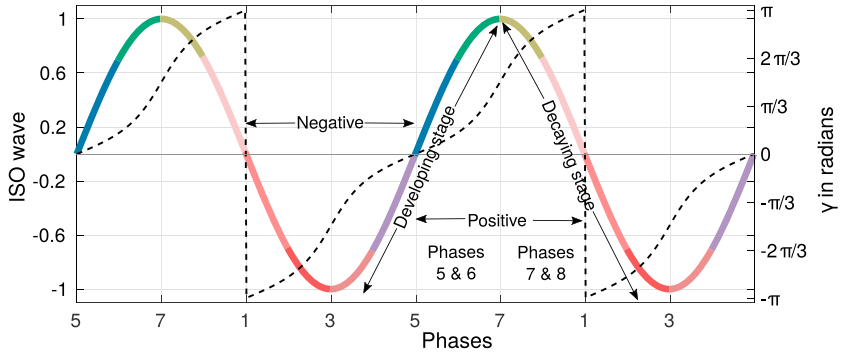

Figure 1. An ideal ISO wave represented by a sine function (solid line; left *y* axis) and associated phase angles (dotted line; right *y* axis). Phase numbers are noted in the *x* axis. Different colors in the ISO wave indicate the eight different phases of ISO. ISO = intraseasonal oscillation.

2.3. Defining Phases of ISO Modes

We determine the phases of ISOs over any location using the oscillatory behavior of LF-ISO or HF-ISO with the help of the following equation:

$$\gamma(t) = Arg(Y'(t) + iY(t)), \tag{3}$$

where t denotes time and $Y(t)$ is the n-day-long LF-ISO or HF-ISO time series over a particular grid point or averaged over a small specified area; $(')$ indicates the time derivative calculated using central differences. $Arg(z)$ represents the principal value of the phase of a complex number $z = x + iy$; $\gamma(t)$ is calculated for each year separately and lies between $-\pi$ and π. Further, we divided the entire phase plane for ISO at any location into 8 equally spaced intervals such that $-\pi + (m-1)\frac{\pi}{4} \le \gamma(t) < -\pi + m\frac{\pi}{4}$, $m = 1, \ldots, 8$. LF-ISO or HF-ISO time series is in phase m if the associated phase angle belongs to the m-th interval. As an illustration, we show an ideal ISO wave mimicked by a sine function in Figure 1. The evolution of the phase angle along with the wave activity is shown by the dotted line and varies from $-\pi$ to π. Phases 1 to 4 corresponds to the negative part of ISO, while phases 5 to 8 are linked with the positive values of ISO. Phases 3 to 6 and 7 to 2 (the eight phases are cyclic in order) can be defined as the developing and decaying stages of ISO, respectively. Based on the values of the phase angle, we can determine the state of the ISO and create phase composite diagrams by taking averages of the days falling into same phases across many years.

In addition, a randomization test is performed in some places to determine the significance of the results. The null hypothesis in this case is that the values observed are coming from a distribution with a zero mean. Then we generated 1,000 bootstrap samples using the observed samples. If 0 is outside the middle 95% of sorted bootstrap samples, then we reject the null hypothesis at 5% significance level.

3. Results

3.1. Local Onset and Demise of the ISM

Figure 2a shows the daily climatology of AIR from the IMD data along with the daily cumulative anomalies. The seasonal evolution of the ISM is observed in the daily time series with rainfall rising during late May through June and shows weakening by the end of September. Based on the cumulative anomalies, the climatological AIR onset date is 2 June and the demise date is estimated as 11 October (Figure 2a). Figures 2b and 2c show the climatological local onset and demise dates. These two panels show the observed progression and retreat of the typical monsoon isochrone between the southern region and the northwest region of India. The central Indian region experiences onset during middle of June. This region exhibits more or less a spatial homogeneity in the occurrences of local onset or demise of the ISM. Since the majority of rainfall over southeastern peninsular India (Tamilnadu) is associated with the northeast monsoon (Rajeevan et al., 2012), this region experiences a very delayed onset. However, central peninsular India (Karnataka) and northeast of India experiences onset very early (as early as mid-April). Wang and LinHo (2002) also suggested that rainfall over northeastern India starts earlier than Indian monsoon itself. Premonsoon showers are often related to the onset over these regions and a smooth transition from premonsoon showers to summer monsoon rains over these regions blurs the distinction between them (Krishnamurti & Ramanathan, 1982; Misra et al., 2017). The premonsoon showers could act as a necessary precursor to the summer rains

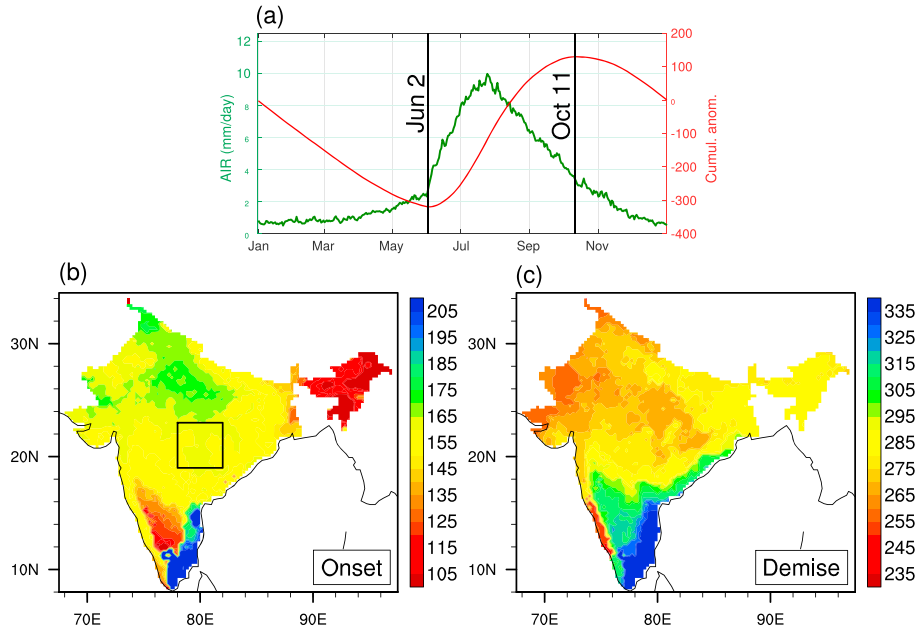

Figure 2. (a) Daily climatology of the AIR (left *y* axis in green) from the observed rainfall data from Indian Meteorological Department and the corresponding cumulative daily anomaly (right *y* axis in red) with the onset and demise dates marked in calendar days. The climatological local (b) onset and (c) demise of the Indian summer monsoon defined at every grid point of the India Meteorological Department gridded rainfall data. The dates are shown in Julian days. The black box in panel (b) marks the central Indian box based on which a case study is made in section 3.4. AIR = all-India rainfall.

over these regions (Misra et al., 2017) and hence are important in understanding the evolution of the ISM. Since determination of onset in this algorithm is based on identifying a smooth monotonous increase in rainfall amount over a location, it detects the onset over these regions very early. Defining onset/demise of the ISM on a local scale bears particular importance to practical applications to understand and anticipate the evolution of the ISM from early onset over parts of peninsular and northeast India.

The climatological local demise of the ISM over CI occurs during late September. Northeast India and parts of peninsular Indian region (except Tamilnadu) experiences the demise mostly by early and late October, respectively. Therefore, with an early onset and a late demise over these areas, the length of the monsoon period is longer than it is over CI. The delayed demise over peninsular India may be associated with the rainfall during the north-east monsoon, which is responsible for rainfall over the southeastern parts of India (Tamilnadu) during the winter months.

3.2. ISO Structure

Intraseasonal variability in the ISM rainfall (June–September, JJAS) is shown in Figures 3a and 3b. The eight phases shown in each figure are calculated based on area-averaged rainfall associated with LF-ISO or HF-ISO over box in CI (19–23° N, 78–82° E). The phase angles are calculated using equation (3). The eight phases showing the basic space-time structure of LF-ISO in Figure 3a are separated from each other by almost 4–5 days and they are cyclic in nature. A positive anomaly starts to develop over southern tip of India in phase 1, with negative anomaly seen over most of central and peninsular India. The positive anomaly moves northward and gets amplified in phases 2 and 3, while a strong dry anomaly is situated over CI. The positive LF-ISO anomaly intensifies and moves further northeastward and reaches CI by phases 6 and 7. In phase 8, the positive anomaly propagates to the foothills of the Himalayas and subsequently weakens over there. The propagating structure of LF-ISO with a northwest-southeast tilt presented here is well documented in many studies (Karmakar et al., 2017b; Krishnamurthy & Shukla, 2007; Lee et al., 2013).

Figure 3b shows the spatiotemporal evolution of HF-ISO. The eight phases shown here are nearly 1–3 days apart from each other. The dominant propagating pattern associated with HF-ISO is observed as a northwestward propagation of convection from the east coast of India to the northwestern region (Karmakar et al., 2017b). Development of a positive anomaly over the eastern coast is seen in phases 4 and 5. This anomaly

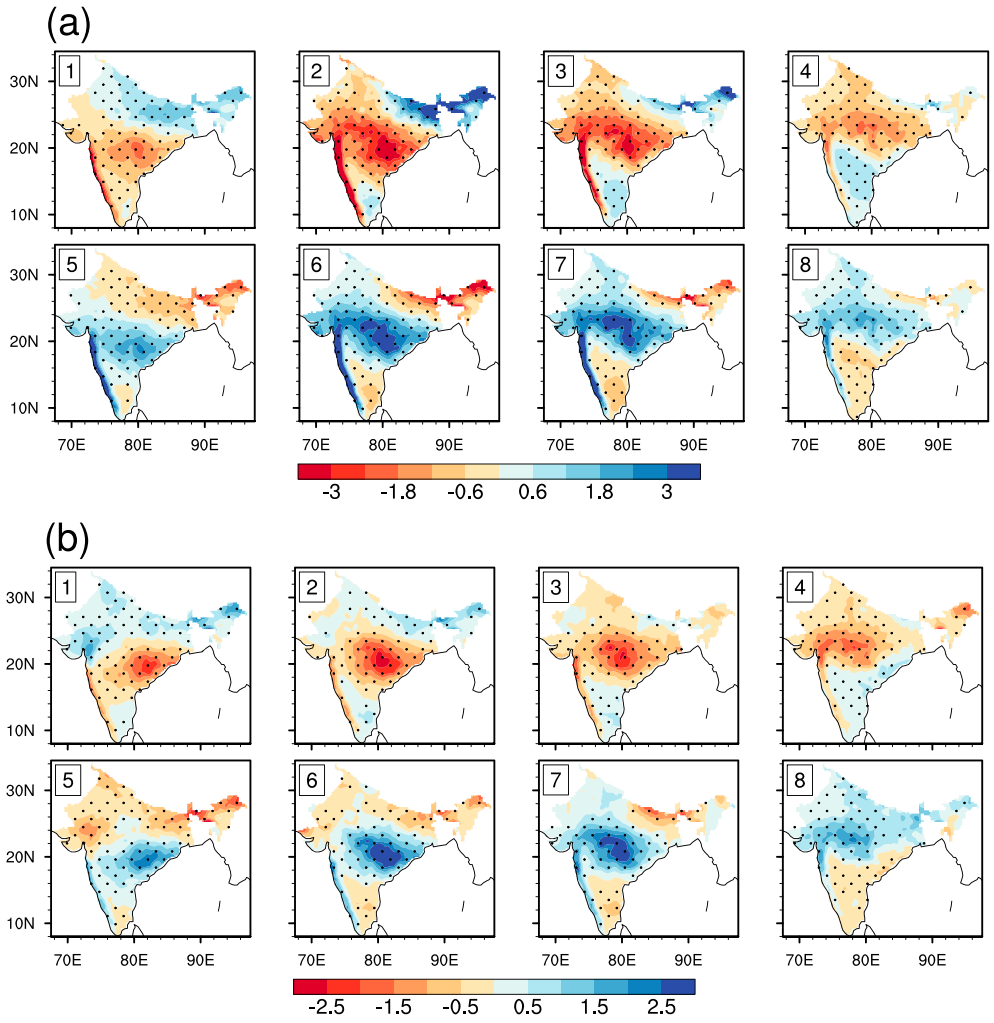

Figure 3. Phase composite diagram for (a) low-frequency intraseasonal oscillation and (b) high-frequency intraseasonal oscillation rainfall (mm/day) during June–September, 1902–2005. The eight phases are calculated based on rainfall over central India as described in the text. Numbers in each panel show the corresponding phase number. Stippled regions indicate where mean is significantly different from 0 at 5% level using a randomization test.

subsequently strengthens and propagates northwestward in phases 6 and 7. Eventually, in phases 8 through 2, this rainfall anomaly moves further westward and dissipates over the northwestern India.

3.3. Onset/Demise and ISO: Analysis on a Local Scale

3.3.1. Progression

Having defined the local onset/demise of the ISM and ISOs, we now examine how the progression of the local onset over India occurs and its relation with these two (LF and HF) modes of ISO. As an illustration, Figure 4a shows the progression of onset of the ISM after 1 June 2005 (a normal monsoon year with weak El–Niño Southern Oscillation effect). On 1 June, local onset has already appeared over parts of peninsular and northeast India (Figure 4a). We note that, local onset over these regions are observed to occur before monsoon onset over Kerala in many years (Misra et al., 2017; Moron & Robertson, 2014; Wang & LinHo, 2002). Onset over Kerala is seen by 9 June, and most of the western Ghats region and western peninsular India experience onset by the third week of June. Onset of monsoon rainfall over the eastern and CI is seen during the last week of June. During first week of July, onset occurs over almost entire India, except the southeast and extreme northern regions of India (not shown).

In Figures 4b and 4c, we show the corresponding gradual progression of LF-ISO and HF-ISO, respectively. During the first three weeks of June, strong negative LF-ISO anomaly is observed over most of southern and CI, which shows a northward propagation (Figure 4b). This negative anomaly gets strengthened over CI by

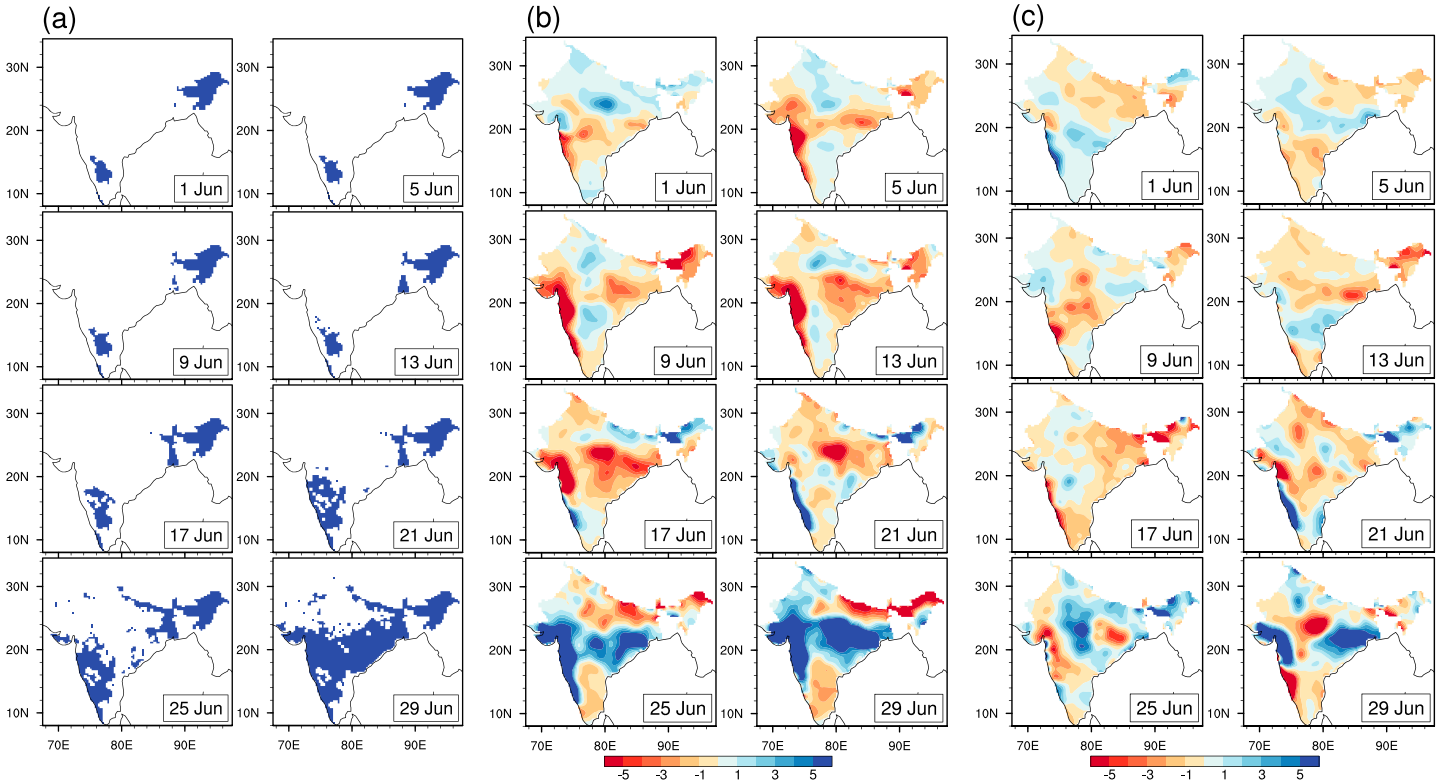

Figure 4. (a) The progression of local onset after 1 June 2005. The shaded area denotes the grid points where onset has already occurred by the indicated day of the panel. The corresponding rainfall anomalies (mm/day) associated with (b) low-frequency intraseasonal oscillation and (c) high-frequency intraseasonal oscillation. Dates are written in bottom right of each panel.

17 June. Gradually, this negative anomaly of the LF-ISO moves further northward and dissipates over the foothills of the Himalayas (last week of June). Onset of monsoon over the CI region does not occur until this negative anomaly starts dissipating. On 13 June, a positive anomaly is seen over peninsular India, which is established over the western Ghats, CI, and northeast regions, and moves further northward between 21 and 29 June. While comparing Figures 4a an 4b, it can be seen that the progression of local onset coincides more closely with propagation of LF-ISO than with the propagation of HF-ISO, at least for this particular example.

Similarly, Figure 4c suggests that onset of the ISM in 2005 over many grid points, especially over the Gangetic plains and the foothills of the Himalayas are triggered by the arrival of a wet lobe of HF-ISO. For example, we note the westward movement of HF-ISO positive rainfall anomalies along 20–30° N during 21 June through 29 June, that is also coincident with local onset in this region (Figure 4a). Likewise, HF-ISO positive anomalies are associated with the occurrence of onset over the western coast of India during the third week of June. Both LF-ISO and HF-ISO show correspondence with the onset over the foothills of the Himalayas by 25 June.

3.3.2. Phase Association

In Figures 5a and 5b, we show an example of LF-ISO and HF-ISO time series over a grid point in CI for 2005 and evolution of its phase, respectively. The local onset and demise dates for the grid point for 2005 are also marked in the figures as vertical lines. The amplitude of LF-ISO and HF-ISO are largest in late June to early October suggesting strong intraseasonal variability during the summer monsoon months. In Figure 5c, we show the actual rainfall over the same grid point over CI and for the same time period in 2005. Although there are some intermittent rainfall during early May, onset of the ISM occurs during the third week of June. Similarly, the demise is noted during the third week of October after a short spell of rainfall. The peaks in rainfall time series coincide with large positive values in LF-ISO and HF-ISO (phases 5–8), which implies that increased amount of rainfall in certain spells over a location can be explained by the combination of the two ISO time series (Karmakar et al., 2017b). Next, we determine the LF-ISO and HF-ISO phases at which

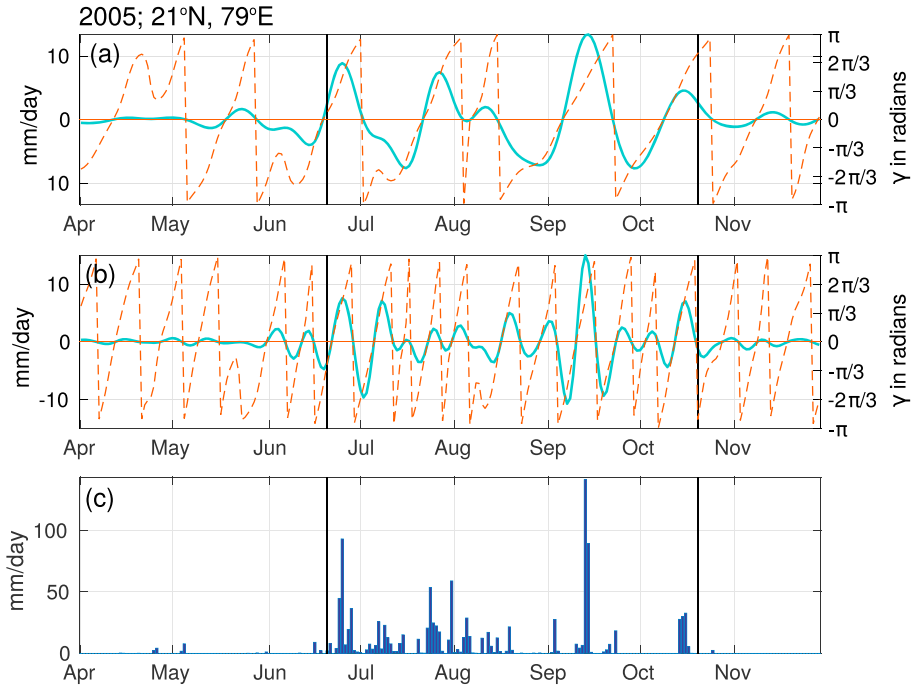

Figure 5. (a) Low-frequency intraseasonal oscillation (left *y* axis; solid line) over a grid point over central India (21° N, 79° E) during April–November 2005 (taken as an example). Right *y* axis shows the phase angle (dotted line) for the same time period calculated as described in the text. (b) Same as (a) but for high-frequency intraseasonal oscillation. (c) Actual rainfall for the same time period over the same location. Local onset and demise dates are shown as vertical lines in all the panels.

the local onset/demise occurred for this location. Phases of the ISO modes are calculated over this grid point using equation (3), and the phase angles are shown in Figures 5a and 5b. Onset of rainfall occurred over this grid point when LF-ISO and HF-ISO are in phases 5 and 4, respectively. Whereas, the LF-ISO and HF-ISO are in phases 8 and 1, respectively, when local demise of the ISM occurred at this grid point. We note that the year 2005 and the location of the grid point are taken just for illustrative purposes in Figures 4 and 5.

Although the space-time evolution of ISOs are seen in Figure 3, we aim to perform phase composite analysis on a grid point basis since we are more interested in investigating the relationship between ISO modes and onset/demise of the ISM on a local basis. This means that although ISO modes posses a large-scale structure, we calculate the phases of the ISO modes at each grid point separately as it is done in Figure 5. Then we analyze the onset/demise events at different phases over each grid point. This basically allows us to understand ISO-onset/demise association in a time-independent manner. For example, let us assume onset of the ISM over a point in southern India happens in phase 2 of LF-ISO as shown in Figure 3a, whereas over a point in northern India it occurs in phase 7 of LF-ISO as depicted in Figure 3a. In both the cases, LF-ISO exhibits a positive anomaly and convectively favorable phase over the respective locations during onset. By this approach, it will be difficult to represent the results in a cumulative form while including all the points in the domain. However, if we can synchronize the LF-ISO phases in both the locations to similar phase, it would provide a better insight on how ISOs on a local scale modulate the occurrence of onset/demise of the ISM.

Figure 6 exhibits the rainfall anomalies associated with the ISO modes if all the grid points over India are phase synchronized. In Figure 6a, we show 104-year composite of LF-ISO associated JJAS rainfall anomalies observed in different phases of ISO at each location. For example, panel 1 in Figure 6a shows the spatial pattern of LF-ISO rainfall anomalies when all the locations are in phase 1 (locally) over India. Since phases are determined at each location separately, panels do not show the space-time evolution of ISO. Rather, Figure 6a shows the LF-ISO pulse in a synchronized way. By definition, strong negative values are observed over the entire Indian region during phases 2 and 3 and positive anomalies are strongest when LF-ISO is in phases 6 and 7. Similar results are seen for composites of the rainfall anomalies in the various phases

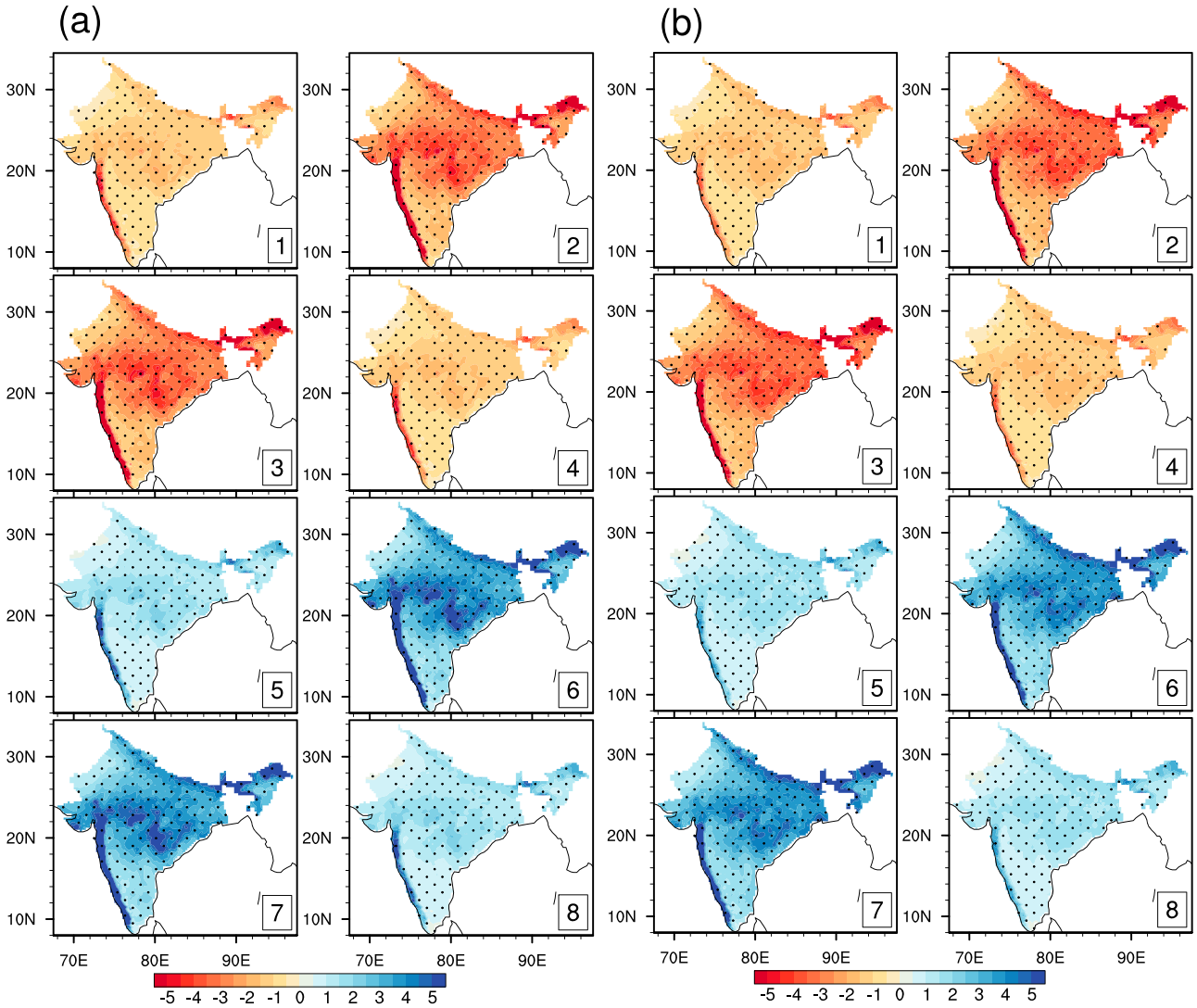

Figure 6. The composite rainfall anomalies (in millimeters per day) associated with the ISO modes if all the grid points over India are phase synchronized for (a) low-frequency ISO and (b) high-frequency ISO for different phases during June–September, 1902–2005. These eight phases are calculated at each grid point separately (see text for details). The phase numbers are noted in the bottom right of each panel. Stippled regions indicate where the values are significant at 5% level using a randomization test. ISO = intraseasonal oscillation.

of HF-ISO in Figure 6b. We note that the regions where the darkest colors are seen in Figure 6 indicate the regions where variance of ISO is maximum. LF-ISO shows more variability over the western Ghats and CI region. In comparison, HF-ISO exhibits strong variability over western Ghats, central and eastern parts of India.

In Figure 7a, we show a histogram of local onset dates for 104 years in different LF-ISO phases considering all the grid points over India. This clearly suggests that phase 5 of LF-ISO is the most preferred phase for onset. It is seen that in Figure 7a that 37.1% of all local onsets occur when LF-ISO is between phases 5 and 6. This suggests that onset is highly favorable when LF-ISO exhibits positive values and positive gradient of its temporal evolution over a location (developing stage of LF-ISO; see Figure 1). Similarly, LF-ISO phases 7 and 8 (positive decaying stage; Figure 1), which contain nearly 39.6% of the total local demise dates of the ISM, are clearly the most preferred phases for withdrawal of the ISM (Figure 7b). A similar relationship between the local onset/demise and phases of intraseasonal activity is noticed when we calculate the distribution for HF-ISO phases (Figures 7c and 7d; 37.4% and 45.2% of the total local onset and demise dates, respectively). Although the distributions show similar characteristics as in Figures 7a and 7b, respectively, the demise dates show higher concentration during phase 7 of HF-ISO.

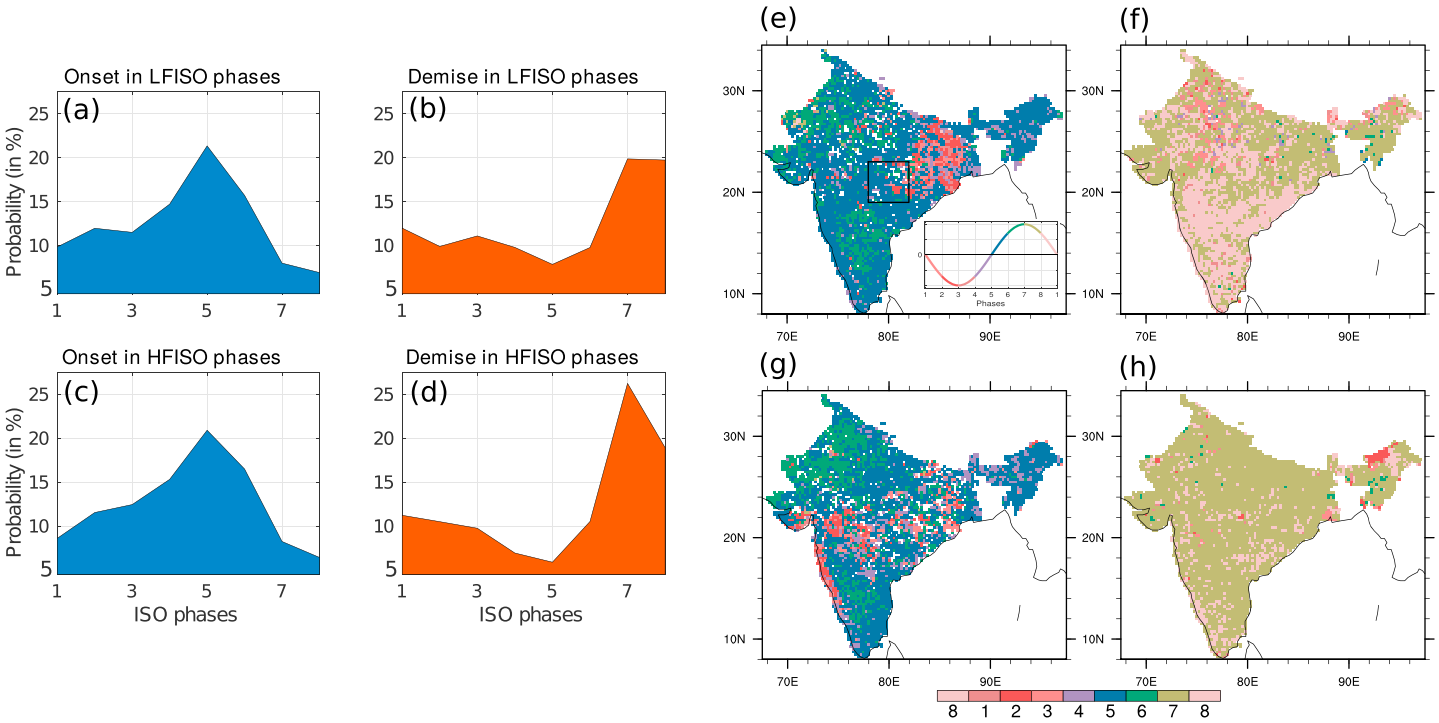

Figure 7. (a) Histogram of local onset dates of the ISM (presented as a percentage of the total) in different LF-ISO phases. All the grid points over the Indian domain considered in this study for 1902–2005 are considered to create the histogram; *x* axis represents different LF-ISO phases, and *y* axis shows the percentage of the total local onset dates that fall in each LF-ISO phase. (b) Same as (a) but for local demise dates of the ISM. (c) Same as (a) but for local onset dates of the ISM in HF-ISO phases. (d) Same as (c) but for local demise dates of the ISM. (e) The spatial distribution of the LF-ISO phase numbers at which the distribution of local onset dates in different LF-ISO phases during 1902–2005 attains maxima. (f) Same as (e) but for the distribution of the local demise dates in LF-ISO phases. (g) Same as (e) but for local onset dates in different HF-ISO phases. (h) Same as (g) but for local demise dates in different HF-ISO phases. Only those grid points are shown in (e)–(h) where the distribution of phases reject the null hypothesis of a uniform distribution at 5% significance level using Kolmogorov-Smirnov Goodness-of-Fit test. The black box in panel (e) marks the central Indian box based on which a case study is made in section 3.4. ISM = Indian summer monsoon; ISO = intraseasonal oscillation; LF-ISO = low-frequency ISO; HF-ISO = high-frequency ISO.

To understand the spatial pattern of this apparent synchronization between onset/demise of the ISM and the phases of ISOs, we plot the peaks (maximum values) of the distribution of ISO phases at which onset/demise of the ISM occurred at each location for the 104-year sample over all India (Figures 7e–7h). In Figure 7e, we observe that most of the points show local onset of the ISM at phases 5 and 6 of the LF-ISO as anticipated from the distribution function in Figure 7e. But there are many locations, especially over the eastern India, where local onset occurrences of the ISM are distributed among LF-ISO phases, which are not favorable for high amount of rainfall (phases 2 and 3). In Figure 7f, we show the spatial pattern of the peaks of the distribution of local demise dates in LF-ISO phases. This suggests that local demise of the ISM mostly occurs during phases 7 and 8 of LF-ISO except in a few regions over northern and northeast India. Similar to LF-ISO, onset/demise of the ISM show strong correspondence with the HF-ISO phases (Figures 7g and 7h). Except few regions, particularly over the western Ghats, occurrence of local onset of the ISM is most favorable during phases 5 and 6 of HF-ISO (Figure 7g). However, demise dates are strongly associated with the HF-ISO phases across entire India and demise of the ISM occurs mostly in phase 7 of HF-ISO except some grid points over northeast India (Figure 7h). Onset of monsoon rainfall occurring in unfavorable phases of LF-ISO over the eastern India coincide with the fact that most of the low-pressure systems that develop over the BoB, in unfavorable LF-ISO phases in many cases, propagate toward this region and cause substantial amount of rainfall during May–early June (Goswami et al., 2003; Karmakar et al., 2015, 2017a). This may mark the onset of the ISM rainfall over these regions just before the low-level westerlies strongly establishes over the domain.

Simultaneous modulation of LF-ISO and HF-ISO modes in the occurrence of local onset/demise of the ISM can be understood using a joint probability distribution plot (Figure 8). In Figure 8a, we show the joint probability distribution for local onset of the ISM in different ISO phases, which clearly shows that the most

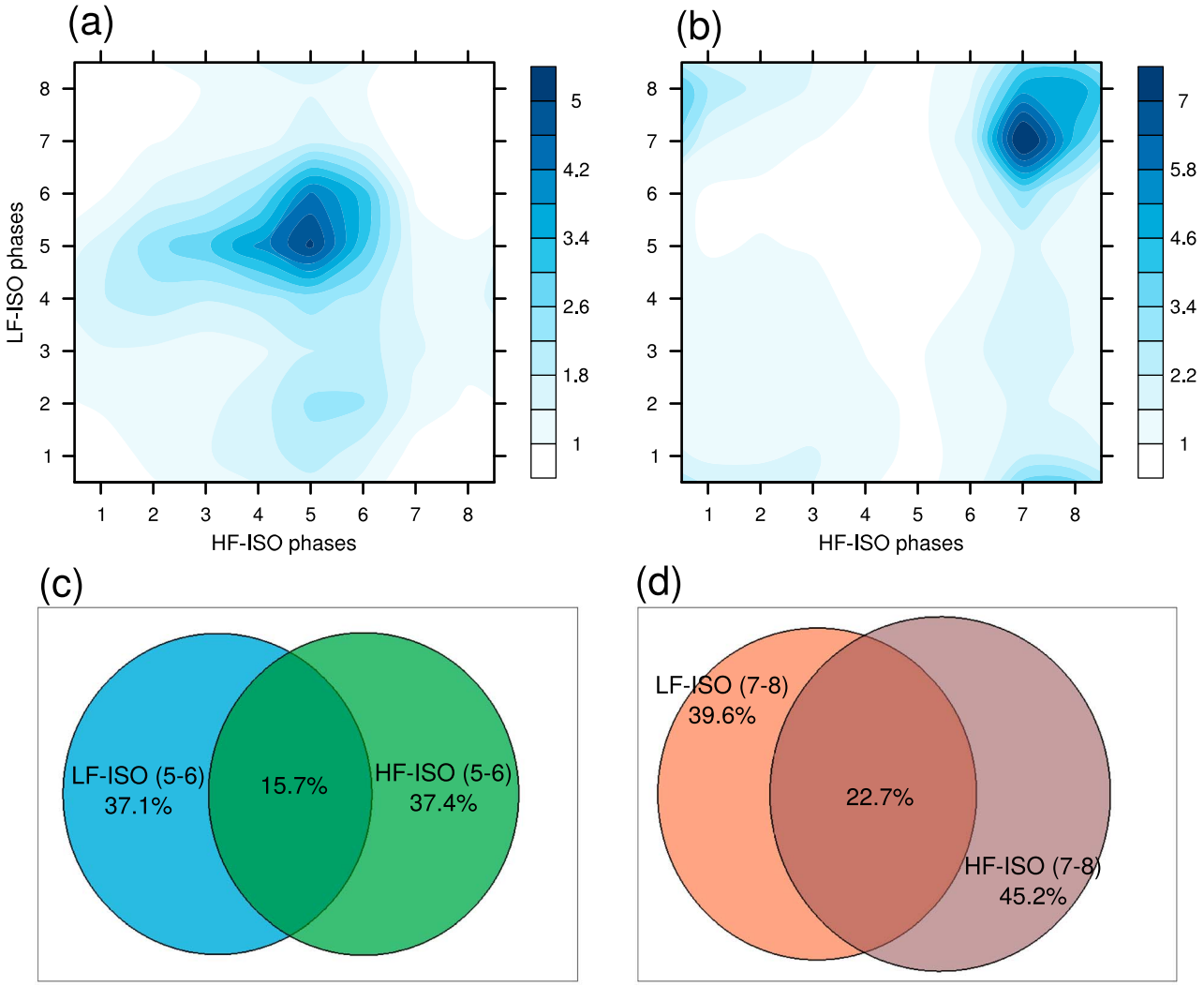

Figure 8. The joint probability distribution (represented as percentage of total occurrences) of the local (a) onset and (b) demise dates of the ISM over the entire domain during 1902–2005 in different LF-ISO and HF-ISO phases. Venn diagrams representing the percentage of occurrence of (c) local onset and (d) local demise over the entire domain in favorable LF-ISO and HF-ISO phases (phases 5 and 6 for local onset and phases 7 and 8 for local demise of the Indian summer monsoon). ISO = intraseasonal oscillation; LF-ISO = low-frequency ISO; HF-ISO = high-frequency ISO.

probable time of local onset of the ISM is when both the ISOs are in phases 5 and 6, a time period of ISO evolution when the rainfall anomalies are growing to their peak positive values. In other words, Figure 8a suggests that the occurrence of local onset is highly coupled with the simultaneous occurrence of wet rainfall anomalies favoring LF-ISO and HF-ISO phases over a given location. However, slightly higher modulation of LF-ISO on local onset can be inferred from observing the slope of the higher probability region in the diagram (Figure 8a). Similar conclusions can be drawn from Figure 8b, where we show the joint probability distribution of the local demise dates of the ISM with the various phases of LF-ISO and HF-ISO. The local demise events of the ISM are highly concentrated when both the ISOs are in phases 7 and 8. These are the phases of ISO when the positive rainfall anomalies associated with ISO are diminishing from its peak positive values (decaying positive stage). Figure 8b also shows a stronger modulation of HF-ISO on the local demise dates of the ISM relative to LF-ISO. This joint probability plots signify the fact that the favorable phase of only one type of ISO may not be the most conducive time for triggering onset/demise over a location. Onset/demise of the ISM highly depend upon the phase locking of both the ISOs (LF- and HF-ISO). In fact, 15.7% of the onset dates are associated with LF-ISO and HF-ISO both being simultaneously in phases 5 and 6 (Figure 8c). Whereas, 22.7% of the total demise events of the monsoon rainfall are linked with the time when both LF-ISO and HF-ISO simultaneously are in phases 7 and 8 (Figure 8d). These percentage values may seem smaller at a glance, but they represent the fact that out of (8 × 8=) 64 combination of LF-ISO and

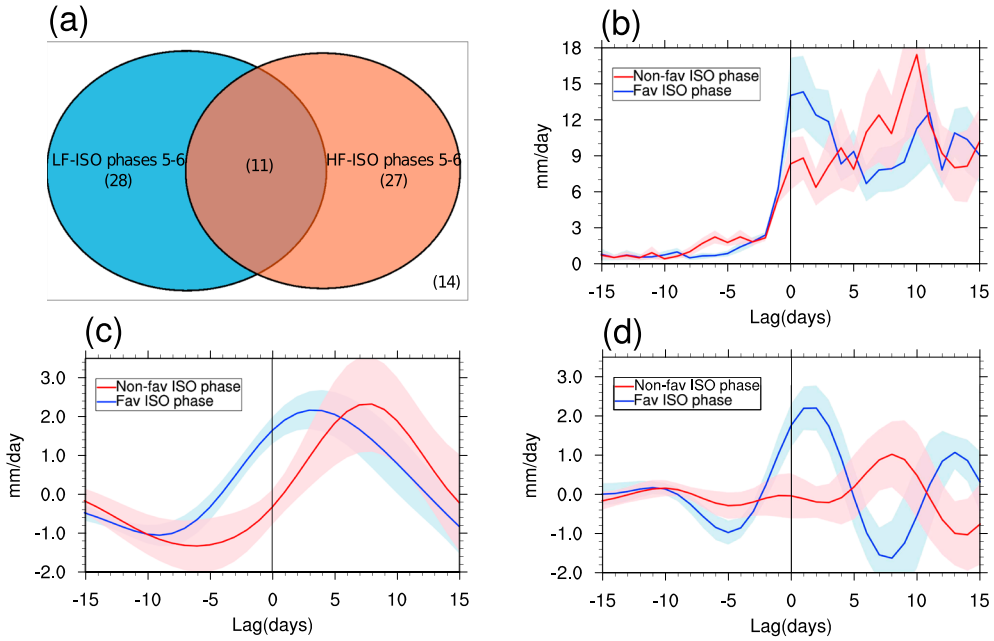

Figure 9. (a) Venn diagram representing the number of occurrence of onset events over CI (19–23° N, 78–82° E) in LF-ISO and HF-ISO phases 5 and 6 during 1948–2005 (58 years). Numbers in parentheses indicate the number of onset occurred in each case. (b) Composite time series of actual rainfall averaged over CI during onset over CI, which occurred when both LF-ISO and HF-ISO are in phases 5 and 6 (favorable ISO phase: Fav case (11 events; blue line) and when neither of LF-ISO and HF-ISO are in phases 5 and 6 (nonfavorable ISO phase: Nfav case (14 events; red line). (c) Same as (b) but for rainfall LF-ISO averaged over CI. (d) Same as (b) but for rainfall HF-ISO averaged over CI. Day 0 (x axis) is the onset date over CI and negative lags indicate days before onset (see text). Shaded areas indicate the spread of the values around the mean at each lag day, normalized by the number of samples. CI = central India; ISO = intraseasonal oscillation; HF-ISO = high-frequency ISO; LF-ISO = low-frequency ISO.

HF-ISO phases, only four capture 15.7% of onset (LF-ISO and HF-ISO phase 5 or 6) or 22.7% of demise events (LF-ISO and HF-ISO phase 7 or 8). A simple, set-theoretic calculation using the Venn diagram (supposing A and B be two sets of numbers and n being the cardinal number: $n(A \cup B) = n(A) + n(b) - n(A \cap B)$) would suggest that 58.8% of the total local onset events fall within phases 5 and 6 (positive developing stage) of either LF-ISO or HF-ISO (Figure 8c). Similarly, 62.1% of the total local demise of the ISM occurred within phases 7 and 8 (positive decaying stage) of either LF-ISO or HF-ISO (Figure 8d).

3.4. Onset Over Central India: A Case Study

Previous analysis substantiates the fact that the ISO modes play a major role in determining the occurrences of local onset/demise of the ISM. In this section, we aim to understand the large-scale flow patterns associated with the ISO modes during the onset of the ISM over CI. We choose CI for this analysis as onset dates over this region is reasonably homogeneous (Figure 2) and also seasonal mean and variance show uniformity (Karmakar et al., 2017b; Rajeevan et al., 2010). Rainfall variability, onset/demise of the ISM over this region is of particular importance to agriculture and water management (Gadgil, 2003). This region is a "climatic hotspot" over south Asia and also one of the most vulnerable regions to the changes in rainfall amount during monsoon season (Mani et al., 2018). Moreover, onset of the ISM is of more socioeconomic interest than the demise.

We use similar approach to identify the onset dates over CI. We consider area-averaged rainfall over a box (19–23° N, 78–82° E; same box used in section 3.2) in this region. The size of the box is chosen in a way so that heterogeneity in local onset dates over a large domain (which may be linked with the progression of the onset isochrone) does not affect the composite analysis and also the box is sufficiently big to bear large-scale features of the region (smoothing out isolated mesoscale systems). Cumulative rainfall anomalies are calculated using the IMD rainfall averaged over this box and onset dates are identified as earlier. JJAS mean AIR and mean rainfall over this CI box show a strong correlation of 0.68. Additionally, onset of the AIR and the monsoon rain over this box are significantly correlated ($R = 0.51$). ISO phases are also determined using equation (3) on the area-averaged LF-ISO or HF-ISO over the box. We use various National Centers for

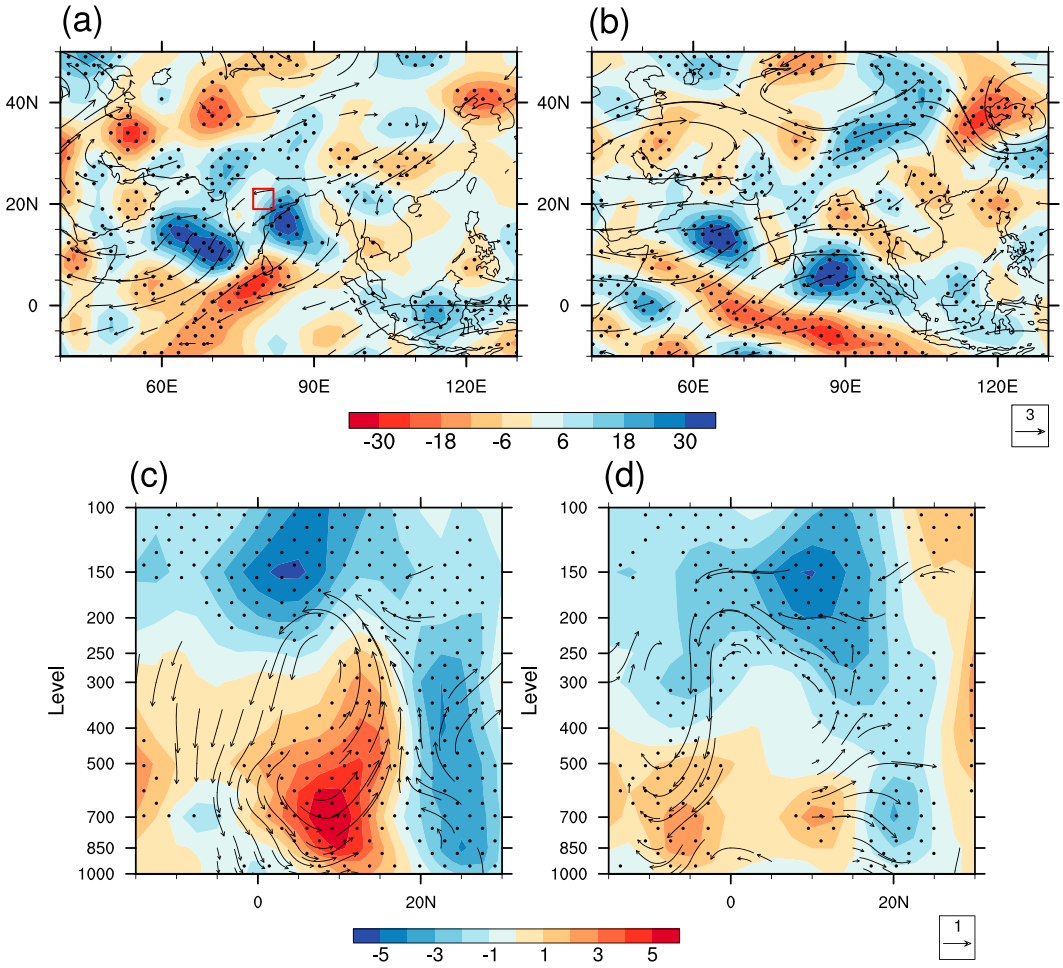

Figure 10. Phase composite of the divergence ($10^7 s^{-1}$) and wind anomalies (m/s) at 200-hPa level during (a) Fav case and (b) Nfav case. Latitude pressure section of composites of zonal wind anomalies averaged between 75–85° E, with vectors of meridional (m/s) and vertical (10^2 Pa/s) wind anomalies during (c) Fav case (11 events) and (d) Nfav case (14 events). All the fields are unfiltered here. Three-day average around the onset date is considered for each onset event (day −1 to day 1, with day 0 as the onset date). Stippled regions indicate values are significantly different from 0 at 5% level using a randomization test. Only those wind vectors are shown that are significant at 5% level. The red box in (a) indicates that the region where averaging is done over central India for this analysis.

Environmental Prediction/National Center for Atmospheric Research Reanalysis-1 products between 1948 and 2005 (58 years) during onset of the ISM over this region to conduct further detailed analysis. Anomalies are calculated in a similar way as described in section 2 and also filtered using MSSA in a similar way to diagnose HF-ISO- and LF-ISO-related fields. These data sets are called as LF-ISO-filtered and HF-ISO-filtered anomalies in the subsequent text.

Out of the 58 cases of onset of the ISM over the CI box, 11 of them occurred when both LF-ISO and HF-ISO are in phases 5 or 6 (developing positive stage). We call these events of onset over CI in ISO favorable phase as *Fav case* (Figure 9a). Whereas, 14 events are there when both LF-ISO and HF-ISO are not in phases 5 or 6. Onset events in these ISO nonfavorable phases are defined as *Nfav case*. Twenty-eight onset events over CI are associated with LF-ISO favorable phase (phases 5 and 6), whereas 27 are associated with HF-ISO favorable phase. Therefore, 44 out of 58 cases (~76%) are associated with either of a favorable ISO phase, which is larger than we found with quarter degree data over all India in section 3.3.2. This could also be attributed to the fact that the analysis over CI is done while considering average over a larger 5° box over CI than 0.25° granular data. Wu et al. (1999) also found in their study that 6 out of 14 years (1980–1993) showed strong contribution of northeastward propagating ISO to the onset of summer monsoon over the South Asian region. The questions we ask here are as follows: What are the spatiotemporal structures of the

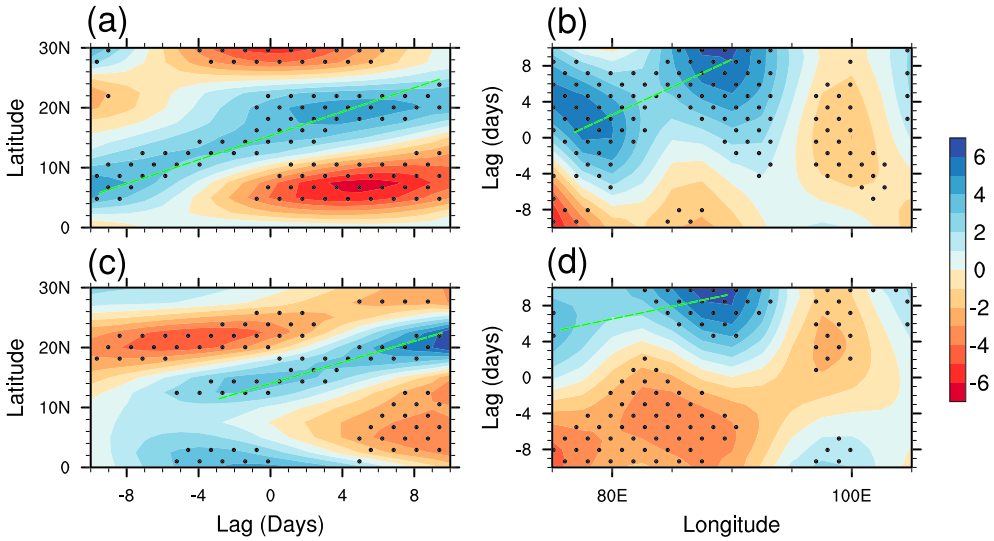

Figure 11. (a) Lag-latitude Hovmöller diagram of low-frequency intraseasonal oscillation-filtered 850-hPa-level vorticity ($10^6 s^{-1}$) during Fav case (11 events). Longitudinal averaging is done over 75–85° E. (b) Same as (a) but for longitude-lag Hovmöller diagram. Latitudinal averaging is done over 15–25° N. (c) Same as (a) but during Nfav case (14 events). (d) Same as (b) but in Nfav case. Day 0 in the *x* axis marks the onset date over central India and negative lags indicate days before onset. Stippled regions indicate values are significantly different from 0 at 5% level using a randomization test. Green slanted lines indicate the northward/eastward propagation.

ISO modes during onset of the ISM over CI? How the atmospheric processes associated with LF-ISO and HF-ISO develop when onset over CI is favored/not favored by them? To address these questions, a detailed comparison between the Fav and the Nfav cases can be very handy. In Figure 9b, we show actual rainfall in the two different cases. A jump in the rainfall amount over CI is seen on the onset date (day 0) in both the cases. However, onset events in the Fav case show more than 1.5 times higher amount of rainfall than in the Nfav case. After the onset, rainfall over CI gradually increases in the Nfav case and almost 10 days later it reaches nearly 18 mm/day. The difference in the rainfall amount is contributed by both rainfall LF-ISO and HF-ISO (Figures 9c and 9d). Both ISOs exhibit developing and positive phase in the Fav case. LF-ISO appears to be phase shifted by around 5 days in the Nfav case, which could have caused the peak in rainfall in that case to arrive at a later date. HF-ISO shows stronger variability during the onset in the Fav case.

In Figures 10a and 10b, we show the upper-level (200 hPa) divergence and wind anomalies (unfiltered) in the Fav and Nfav cases, respectively. The composite diagrams show 3-day mean around the onset dates. Therefore, $11 \times 3 = 33$ days are used in the composite in Figure 10a and $14 \times 3 = 42$ days in Figure 10b. In all the cases (in Figure 10 and henceforth), 1,000 bootstrap samples are generated to test the significance of the observed mean as discussed in section 2. The significance of the results are also tested using two-tailed *t* test against a null hypothesis of zero mean (not shown) and the conclusions remain unchanged. In Figure 10a, strong divergence anomalies are seen over the BoB and the AS, almost entire Indian region and also over the maritime continent. Anticyclonic flow over the Tibetan region is established with strong upper level easterlies are seen over the Indian region. In Figure 10b, divergence anomalies over the Indian region is comparatively weaker and is shifted southward over BoB. Tibetan anticyclone is not established with the anomalous subtropical westerly jet stream located over 35° N. Monsoon onset over India is often associated with the shift in the subtropical westerly jet to the north of the Tibetan Plateau (Schiemann et al., 2009). It is also seen that the anomalous easterly flow over CI is weaker in the NFav case than in Fav case. This suggests that large-scale anomalous upper-level circulation is well established for monsoon onset in the Fav case than in NFav case.

The latitude-pressure section of zonal wind anomaly (unfiltered) is shown in Figure 10c for the Fav case, with vectors showing the meridional and pressure velocity anomalies. The same for the Nfav case is shown in Figure 10d. The zonal wind anomaly over the Indian region is westerly and easterly to the south and north of approximately 18° N, respectively. Zonal wind anomalies from the surface to almost 200 hPa show strong signal in the Fav case as compared to the Nfav case, suggesting the establishment of strong cyclonic

vortex over the CI region in the Fav case. Upward vertical velocity is seen over 15–20° N, and the downward branch is located near the equator in the Fav case and slightly to the south of the equator in the Nfav case. This Hadley cell circulation is much stronger in the Fav case than in Nfav case. The vertical structure of the zonal wind associated with the convection center over CI during onset penetrates deeper into the upper troposphere in the Fav case. Comparatively, the vertical structure appears weaker and limited within the midtroposphere from surface in the Nfav case. Also, it can be inferred that the vertical shear of zonal wind over CI is higher in Fav case than in Nfav case mostly because of more intense lower level winds in the Fav case.

3.4.1. LF-ISO Progression

To understand how progression of LF-ISO is associated with the onset over CI, we analyze LF-ISO-filtered 850-hPa-level vorticity. The composite Hovmöller diagram for Fav case presented in Figure 11a shows that the onset over CI coincides with a northward propagation of low-level vorticity, which propagates from near the equator to the foothills of the Himalayas within a month time. An eastward component associated with the propagation is also observed along the CI region (Figure 11b). In the Nfav case, the northward-propagating vorticity anomaly is weaker over CI during onset and does not seem to originate over the equatorial region (Figure 11c). Northward movement is seen after day 0 (onset) from around 12° N, which intensifies at day 10 over the CI region. This could be related with the rainfall peak in Nfav case 10 days after the onset (Figures 9b and 9c). Eastward propagation is also observed, which is weak during onset (day 0) but intensifies at lag 10 over 85–90° E (Figure 11d).

Vorticity plays an important role in the northward propagation of the convective anomalies over the Indian domain during monsoon. Jiang et al. (2004) suggested that in the presence of strong easterly vertical shear during monsoon, barotropic vorticity is generated to the north of the convection center, which leads to the genesis of barotropic divergence in the free atmosphere. This in turn, helps boundary layer convergence to the north of the convection center and thereby moving convection further northward. Therefore, strong northward propagation of LF-ISO-filtered vorticity anomalies from the equatorial region in Figure 11a explains the strong LF-ISO rainfall over CI during onset in the Fav case. Presence of strong easterly vertical shear during onset in the Fav case can also be inferred from Figure 10c. However, we note that the AS region experiences strong positive low-level vorticity anomaly (LF-ISO filtered) nearly 7 days before the onset over CI in both Fav and Nfav cases (supporting information Figure S1). This anomalous cyclonic vortex propagates northward in subsequent days and the vortex center moves to almost the same latitude as of the CI box on the day of onset over CI. However, whereas the size of this cyclonic vortex is well-stretched over the BoB in the Fav case, it is restricted within the AS in the Nfav case. The positive vorticity anomaly over the BoB is located near the equator with a weaker meridional extent to the central BoB during the onset in the Nfav case (Figure S1). This moves northward in few days after the onset (not shown) and is associated with rainfall peak on day 10 after the onset in this case. The generation of cyclonic vortex over the AS before the onset over CI in both the cases follows the results presented in Krishnamurti and Ramanathan (1982), where they suggested an increase in the kinetic energy of the total flow and the nondivergent component of the flow over the AS almost 7 days before the onset of rainfall over CI, which gradually moves northward along with the differential heating signal between the land and sea. Therefore, our results suggest that the onset events over CI in both the cases are primed by the generation of a cyclonic vortex over the AS 7 days before the onset, but this development is associated with a well-marked large-scale positive vorticity anomaly stretched over the AS and BoB in LF-ISO time scale in the Fav case. This large band of vorticity is associated with the developing strong positive LF-ISO rainfall over CI during the onset in the Fav case.

Northward propagation of convective bands from the equatorial region to the CI region are often preceded by an anomalous surface temperature pattern (Karmakar et al., 2017b; Kemball-Cook & Wang, 2001; Klingaman et al., 2008; Sengupta et al., 2001). It is suggested that SST anomalies are nearly in quadrature with precipitation, with warm SST over the northern BoB and AS leads rainfall anomalies by approximately 10 days. Fluctuations in the net heat flux at the ocean surface leads the surface temperature anomalies, which are associated with northward moving active/suppressed convection. In Figure 12a, we show LF-ISO-filtered SST and land skin temperature anomalies overlayed with 850-hPa winds 9–11 days before the onset in the Fav case. Significantly strong positive anomalies are seen over CI stretching further northwestward. Significant positive anomalies are also seen over the Indonesian region, suggesting a possible large-scale pattern of surface temperature oriented in a northwest-southeast direction. Wind anomalies show a significant presence of a cyclonic vortex over the southern Indian region centered at around 10° N flanked toward both the

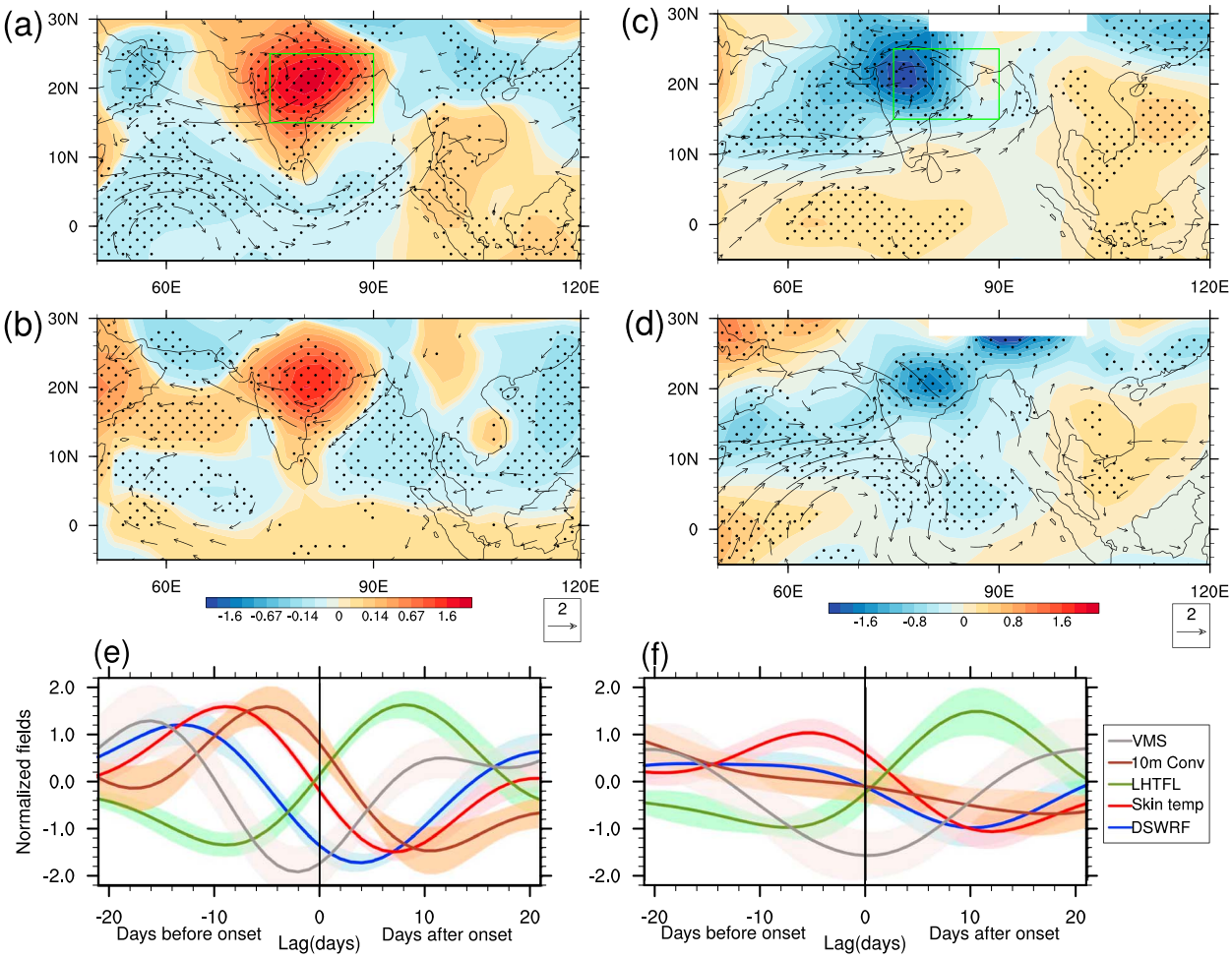

Figure 12. LF-ISO-filtered skin temperature (sea surface temperature and land skin temperature; in kelvins) and 850-hPa wind (m/s) anomalies during 9–11 days before onset over CI occurring in (a) Fav case and (b) Nfav case. Note the nonlinear color bar. LF-ISO-filtered VMS (kJ/kg) and 850-hPa wind (m/s) anomalies during onset (−1 to +1 days) over CI in (c) Fav case (11 events) and (d) Nfav case (14 events). Stippled regions indicate values are significantly different from 0 at 5% level using a randomization test. Wind anomalies significant at 5% level are shown. Composites of LF-ISO-filtered downward shortwave radiation flux at surface, skin temperature, LHTFL at surface, 10-m convergence, VMS averaged over a box over CI (shown in panels a and b) are shown for different days during onset (e) Fav case and (f) Nfav case; *x* axis represents time with day 0 is the onset date over CI and negative (positive) lags indicate days before (after) onset. All the fields in (e) and (f) are divided by standard deviation of the respective fields in Fav case to compare with one *x* axis. Standard deviation of downward shortwave radiation flux, skin temperature, LHTFL, 10-m convergence, and VMS are 12.13 W/m^2, 0.73 K, 10.18 W/m^2, 5.44 × 10^{-7}s^{-1}, and 0.58 kJ/kg, respectively. Shaded areas indicate the spread of the values around the mean. CI = central India; LHTFL = latent heat flux; LF-ISO = low-frequency intraseasonal oscillation; DSWRF = downward shortwave radiation flux; VMS = vertical moist stability.

southern BoB and AS. Figure 12b shows the same anomaly field 9–11 days before onset in the Nfav case. In this case, the large-scale pattern in skin temperature is not seen, except a strong positive anomaly over CI with negative anomalies over the BoB region. Northwest-southeast tilted structure in not seen in this case as SST over the maritime continent shows insignificant patterns. The strong cyclonic vortex over the southern Indian region is also not seen in the Nfav case.

We estimate the stability of the atmosphere by calculating the vertical moist stability (VMS) at each grid point. VMS is defined as the difference between the vertically integrated moist static energy of the upper troposphere and the lower troposphere (Neelin & Held, 1987). The middle of the atmosphere is taken as 600 hPa. Increase in VMS would suggest a stable atmosphere, and lower VMS provides indication toward existence of deep convective cloud structures (Srinivasan & Smith, 1996). In Figures 12c and 12d, we show LF-ISO-filtered VMS and 850-hPa wind anomalies during onset over CI in the two cases, Fav and Nfav, respectively. In Figure 12c, a large-scale strong significant structure of negative VMS anomalies over the CI region flanked over the adjacent oceans is seen. Associated with that, the LF-ISO-filtered low-level winds show an establishment of strong cyclonic circulation pattern over the CI region with strong westerlies over

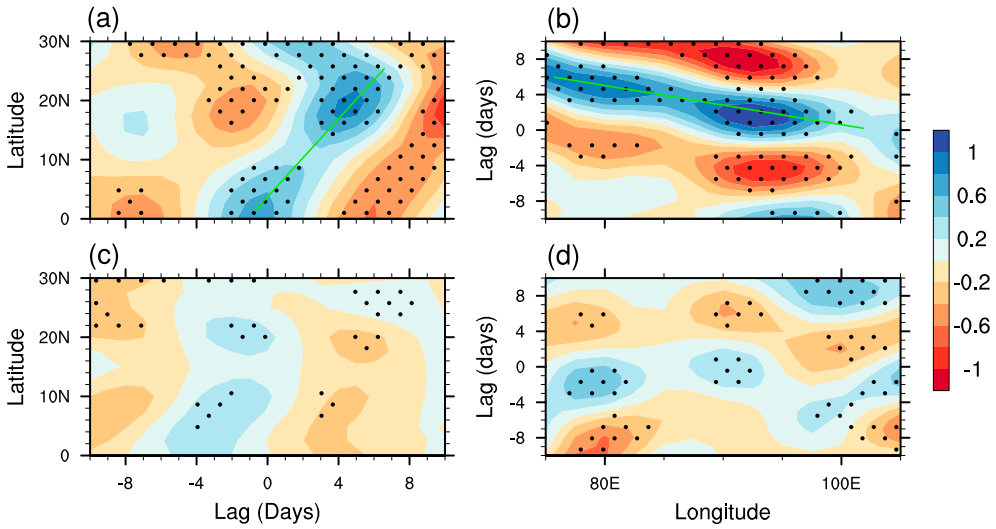

Figure 13. (a) Lag-latitude Hovmöller diagram of high-frequency intraseasonal oscillation-filtered 850-hPa-level meridional wind (m/s) during onset in Fav case (11 events). Longitudinal averaging is done over 75–85° E. (b) Same as (a) but for longitude-lag Hovmöller diagram. Latitudinal averaging is done over 16–26° N. (c) Same as (a) but during onset in Nfav case (14 events). (d) Same as (b) but during onset in Nfav case. Day 0 marks the onset date over central India and negative lags indicate days before onset. Stippled regions indicate values are significantly different from 0 at 5% level using a randomization test. Green slanted lines indicate the northward/westward propagation.

the peninsular India. This large-scale vortex essentially moved northward from southern Indian region (as seen in Figures 12a and S1). This is again indicative that the onset in this case is associated with a development of a large-scale convectively unstable atmosphere over the region. Positive VMS anomalies are seen over the equatorial Indian Ocean, which again, is associated with the descending branch of the Hadley cell circulation. On the contrary, in the Nfav case, we observe the VMS anomalies show weaker patterns over CI (Figure 12d). Furthermore, in the Nfav case, the westerlies bifurcate over the western Ghats and the formation of large-scale anomalous circulation appears different from climatological monsoon flow.

The time evolution of the LF-ISO mode before the onset over CI is revealed in Figure 12e, where we show different reanalysis terms averaged over a box in the region (the size of the box for these terms is intentionally kept bigger than the CI box used in this study as the reanalysis data are of coarser resolution; the conclusions are insensitive to slight changes in the size of this box). Clearly, almost 16 days before the onset over CI, atmosphere becomes stable (increased VMS) followed by an increase in downward shortwave radiation flux (DSWRF) anomaly. The increase in DSWRF results into increase in positive skin temperature anomaly over the region nearly 8–10 days before onset over CI. Increase in skin temperature immediately affects the latent heat flux (LHTFL) anomaly at the surface and a decrease in LHTFL is observed, suggesting the transfer of moisture from the surface to the atmosphere. This is followed by a formation of 10-m convergence, which peaks by approximately 5 days before the onset. Lead of convergence before the initiation of rainfall during onset over CI is also consistent with the properties of Madden-Julian Oscillation (MJO) propagation near the equator (Hendon & Salby, 1994). This increase in moisture in the atmosphere and low-level convergence lead the atmosphere become unstable, as the VMS attains minima just 2 days before the onset. The instability results into the development of deep convection and strong rainfall associated with it over the CI box while triggering the onset (as seen in Figures 9b and 9c). The generation of negative LHTFL anomaly 8 days before the onset suggests that the surface fluxes (air-sea interaction) may play a crucial role in conditioning the atmosphere for the LF-ISO mode to propagate in the Fav case. Negative LHTFL anomaly weakens the widespread positive stability of the atmosphere and supplies moisture to the atmosphere, which builds up the atmosphere for the arrival of a low-level convergence. After the onset, a significant increase in LHTFL anomaly is seen, with the atmosphere becoming stable within 10 days after the onset. Subsequently, increase in DSWRF is seen and next phase of LF-ISO cycle begins.

The Nfav case also shows signals of positive DSWRF, skin temperature before the onset, but they are very weak as compared to the Fav case (Figure 12f). Negative LHTFL is also observed 6 days before the onset, but the 10-m convergence is not seen. In fact, convergence over the region remains negligible before the

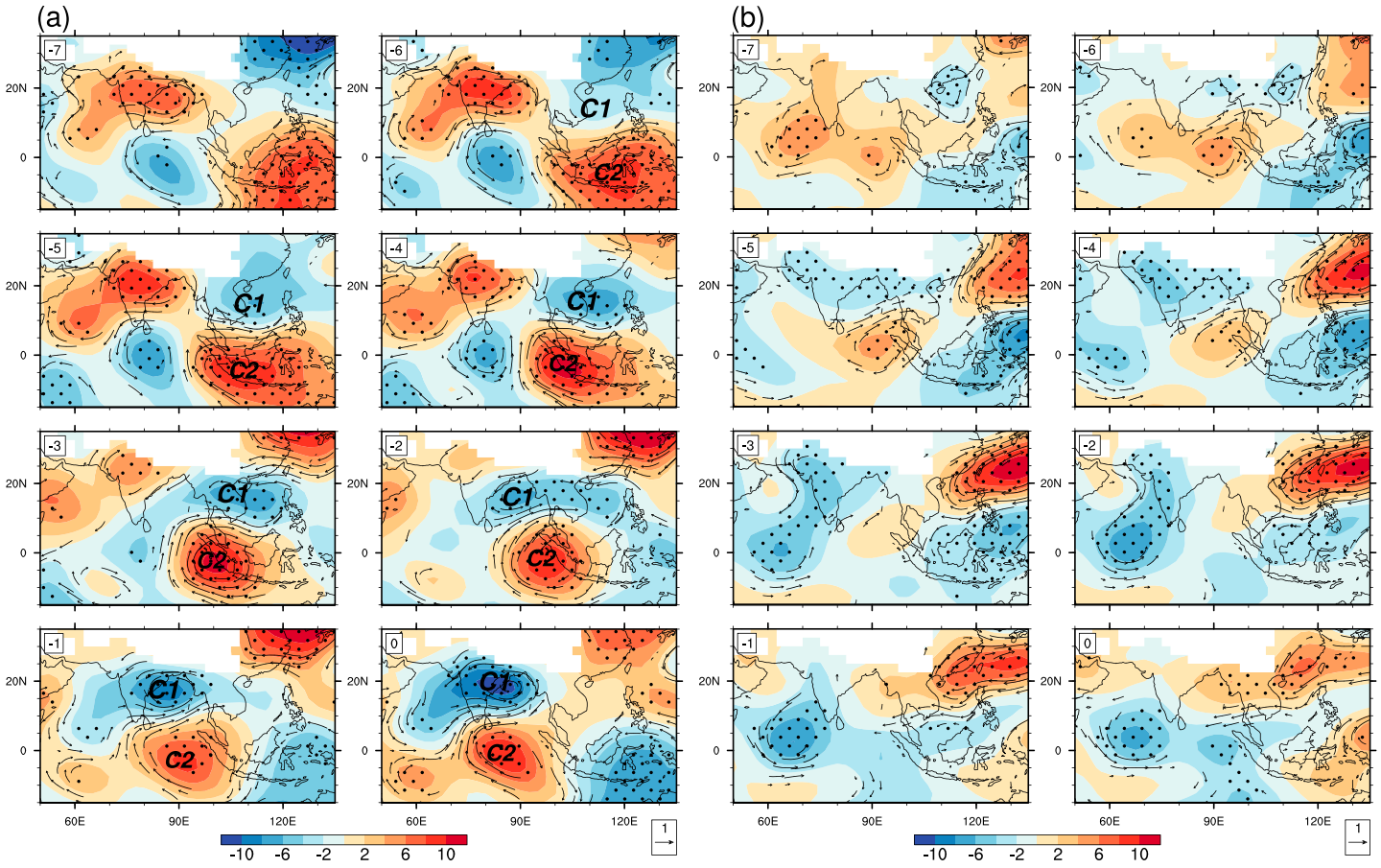

Figure 14. Spatial patterns of high-frequency intraseasonal oscillation-filtered streamfunction (10^{-5} m^2/s) and wind (m/s) anomalies at 850-hPa level before and during onset over central India in (a) Fav case (11 events) and (b) Nfav case (14 events). Numbers in top-left corner of each panel suggest days before onset (day 0 is the onset date). Stippled regions indicate values are significantly different from 0 at 5% level using a randomization test. Wind anomalies significant at 5% level are shown. Letters "*C*1" and "*C*2" in panels in (a) indicate the approximate locations of the centers of the low-pressure cells as discussed in the text.

onset. However, increased skin temperature and negative LHTFL anomalies lead to an unstable atmosphere, albeit weak, in phase with the onset. Maxima/minima in skin temperature or LHTFL anomalies in the Nfav case are seen 3–4 days later as compared to Fav case, suggesting LF-ISO cycle is phase shifted by few days in the Nfav case, which was also seen in Figure 9c. However, the results in Figure 12e case suggest that LF-ISO evolution plays an important role in modulating the onset over CI in the Fav case. The LF-ISO propagation characteristics presented here, especially in the Fav case, are consistent with the previous studies that proposed mechanisms of northward propagation of convection from the equator (Jiang et al., 2004; Kemball-Cook & Wang, 2001).

3.4.2. HF-ISO Progression

The 10- to 20-day mode also plays an important role in modulating the rainfall over CI (Chen & Chen, 1993; Karmakar et al., 2017b; Krishnamurti & Ardanuy, 1980; Krishnamurti et al., 1985; Murakami, 1976). Initial studies on the 10- to 20-day mode suggested a westward propagation from the westernmost Pacific to the Indian monsoon trough. We find that this mode also plays a role in the onset of monsoon rainfall over CI. Figures 13a and 13b show the composite $y - t$ diagram of HF-ISO-filtered meridional wind anomalies at 850-hPa level over 75–85° E and the $x - t$ diagram of the same over the central Indian region, respectively, for the Fav case onset events. Clearly, a strong westward propagation is observed with a northward component associated with it. Chatterjee and Goswami (2004b) showed that the mean spatial structure of this westward propagating mode in circulation and convection "resembles that of a gravest meridional mode equatorial Rossby wave with wavelength of about 6000 km and westward phase speed of approximately 4.5 m/s." However, in the Nfav case, we do not see any westward propagation of meridional wind anomalies in the 10- to 20-day time scale (Figure 13d). Moreover, although there is a very weak signature of northward propagation

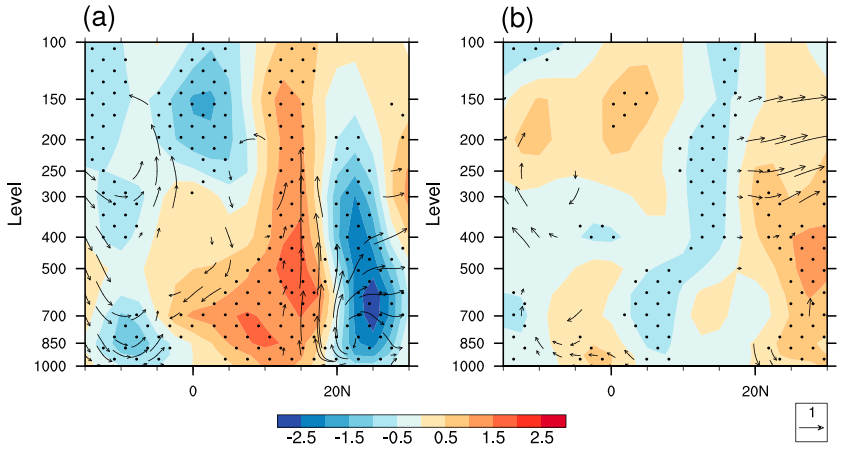

Figure 15. Latitude-pressure section of composites of high-frequency intraseasonal oscillation-filtered zonal wind anomalies along 85° E, with vectors of high-frequency intraseasonal oscillation-filtered meridional (m/s) and vertical (10^2 Pa/s) wind anomalies during onset over central India in (a) Fav case (11 events) and (b) Nfav case (14 events). Three-day average around the onset date is considered for each onset event (day −1 to day 1, with day 0 as the onset date). Stippled regions indicate values are significantly different from 0 at 5% level using a randomization test. Wind anomalies significant at 5% level are shown.

just north of the equator (Figure 13c), the phase of the *v*-wind anomalies are almost in quadrature to the ones observed in Fav case (Figures 13a and 13c and Figures 13b and 13d).

In Figure 14a, we show the composite spatial structures of HF-ISO-filtered streamfunction and wind anomalies at 850 hPa level for different days before onset over CI in the Fav case. The synoptic structure of 10- to 20-day mode makes streamfunction an informative variable. Clearly, almost 6 days before the onset, two cells form along 115° E: one over the South China Sea, one just south of the equator. The movement of the northern cell is also documented in the $x - t$ diagrams of Krishnamurti and Ardanuy (1980) from the westernmost Pacific region. The center of the cell intensifies as it moves westward. The center moves to the BoB 2 days before onset while negative streamfunction values also being observed over the Myanmar region. A closed circulation pattern is also seen. The cell intensifies more on day-(-1), one day before onset, and enters into the CI region. During onset, the center gets established over CI and stretches across the AS. Clearly, the onset in the Fav case is modulated by the arrival of this cell from the western Pacific.

Along with the westward propagating northern cell, we also find a southern cell moving westward along the equator just before the onset in the Fav case. A positive streamfunction anomaly is seen over the New Guinea region 7 days before onset over CI (day-(-7)), which gradually moves westward while coupling with the northern cell. On day-(-2), it moves over the Sumatra coast and eastern equatorial Indian Ocean. On the day of onset, it gets established over the central equatorial Indian Ocean and the southern BoB. Thereafter, both the cells move slightly northwestward and diminishes in 3–4 days over the northern AS (not shown). This northwestward movement can also be seen from the signals of opposite sign in day-(-6) to day-(-1). This westward propagation of cyclonic cells from the western Pacific is not seen in the NFav case (Figure 14b). In fact, although insignificant, streamfunction anomalies of opposite sign compared to the Fav case is seen over CI and the BoB during onset (day 0). However, there exist a significant negative anomaly over the southern AS just before and during the onset.

Existence of this double-cell structure during boreal summer and its westward propagation in the 10- to 20-day time scale was also documented in Chen and Chen (1993). Further, both Murakami (1976) and Chen and Chen (1993) suggested that this 10- to 20-day mode does not show phase change in its vertical structure. As suggested by Figure 14a for the double-low system during onset in the Fav case, low-level easterlies (westerlies) exist in the northern side of the northern (southern) cell. The signs of the zonal wind anomalies are opposite in the southern sides of each cell. This is also seen in Figure 15a, where we show latitude-pressure section of HF-ISO-filtered zonal wind anomalies along 85° E during the onset over CI in the Fav case. The corresponding meridional and vertical velocities are also shown in Figure 15a. In the northern cell, HF-ISO-filtered zonal wind anomalies show the structure stretched up to the top of the troposphere, where as the southern cell is confined within almost 300 hPa. Northern cell is more intense than the southern cell

in terms of zonal winds as well as in vertical winds. These structures support the results presented in Chen and Chen (1993), suggesting that the arrival of a well-structured 10- to 20-day mode is associated with the onset over CI in the Fav case. However, these structures are missing the Nfav case (Figure 15b). Similar to the conclusions drawn from Figures 13 and 14, not only the magnitude is weaker and insignificant, the phase of the zonal wind anomaly is also opposite in this case than in Fav case.

This case study basically highlights the importance and mechanism of the ISO modes in modulating the onset of summer monsoon rainfall over CI and the structures of these modes before and during onset. Clearly, not all the onset events are triggered by the arrival of ISO modes. Eleven out of 58 happened when both the modes favored, 14 of them occurred when both the ISO modes do not exhibit developing positive stage. However, there are $28 - 11 = 17$ and $27 - 11 = 16$ cases of onset when either only LF-ISO or only HF-ISO is in favored phase, respectively (Figure 9a). The structures of the atmospheric columns as revealed by the LF-ISO- and HF-ISO-filtered data in these 17 and 16 cases, respectively, are similar to the figures shown here (not shown). We also analyzed few other regions (eastern India, northeast India, northwestern India, and the western Ghats) in a similar way as it is done here and the dominance of the ISO modes during onset in each region are examined (supporting information Figures S2–S5). We found ISO modes, especially LF-ISO, play weaker role over eastern India and stronger role over the western Ghats during onset. HF-ISO plays important role over the northeast India.

4. Conclusions and Discussion

In this study we examined the relationship of the local onset and demise of the ISM with intraseasonal variability using observed rain gauge analysis over the Indian subcontinent for 104 years. We calculated the inflexion points in the cumulative rainfall anomaly at each grid point and then anchored it to the AIR to find out the local onset and demise dates. A data-adaptive technique (MSSA) is used to identify two types of ISO modes: northward-propagating LF-ISO and northwestward-propagating HF-ISO. An analysis, considering each grid point separately, showing the association between onset/demise of the ISM and ISO modes are presented here. This study provides a quantitative measure on the modulation of ISO phases on the occurrences of local onset or demise of the ISM.

The influence of the ISO modes on local onset/demise of the monsoon rainfall is seen as majority of local onset occurring in phases 5 and 6 of both HF-ISO and LF-ISO, which signifies a phase of ISO when the positive rainfall anomalies are growing to their peak value (positive and developing stage). Similarly, the influential role of ISOs on the local demise of the ISM is diagnosed when a large fraction of local demise of the ISM occurs during phases 7 and 8 of LF-ISO and HF-ISO, a phase of ISO when the rainfall anomalies are diminishing from its peak positive values (positive decaying stage). A simple calculation from the Venn diagram (Figure 8) suggests that 58.8% of the total local onset events fall within phases 5 and 6 (positive developing stage) of either LF-ISO or HF-ISO. Similarly, 62.1% of the total local demise events occurred within phases 7 and 8 (positive decaying stage) of either LF-ISO or HF-ISO. The phase locking between the two ISO modes plays a significant role in modulating the seasonal progression of the ISM (as observed in Figures 8a and 8ab), especially with the local demise (22.7% of all local demise occurs when both LF-ISO and HF-ISO are simultaneously in phases 7 and 8) as compared to local onset (15.7% in phases 5 and 6). Given the high granularity of the data set (0.25° data), this analysis show a remarkable association between the ISO modes and onset/demise of the ISM. There are, however, significant portions within the core of the ISM where both its local onset and demise occur in the unfavorable phases of the ISO. For example, occurrence of local onset over the parts of eastern India are associated with negative LF-ISO phases (phases 2 and 3). Similarly, most probable time for local onset over the parts of western Ghats is when HF-ISO is in negative phase (Figure 7g). This regional heterogeneity in the relationship between ISO and onset/demise of the ISM is interesting and needs to be understood further to unravel the relationship between the seasonal envelope and the finer spatiotemporal structures of the ISOs. It is also suggestive that the performance of the numerical models that are used to predict the behavior of the ISM and its onset/demise is dependent upon how it simulates the ISO modes.

We also present a case study to show how large-scale atmospheric structures are associated with onset of the ISM over CI. It is found that when onset of the monsoon rain occurs with both ISOs over CI are in phases 5 and 6 (Fav case), strong low-level westerlies are seen over the southern Indian region with westerlies to the north of CI. The subtropical westerly jet gets established to the north of the Tibetan Plateau

and an upper-level anticyclone is observed over Tibet. This is accompanied by a large-scale anomalous convective structure over the Indian region with a strong Hadley cell circulation. Establishment of this pattern is preceded by an increased anomalous DSWRF, strong positive surface temperature anomaly, and negative LHTFL anomaly at the surface over the CI region in LF-ISO time scale. The large-scale patterns are tilted in a northwest-southeast direction and stretched from India to the maritime continent. Increased surface convergence 2–3 days before the onset helps destabilizing the atmosphere in the presence of enhanced moisture, which leads to initiate the onset of rainfall over CI. The low-level LF-ISO-filtered positive vorticity structures show strong northward propagation from near the equator starting from almost 15 days before the onset, which arrive CI during the onset. The results presented in this case before the onset support the existing ideas of northward propagation of convection at LF-ISO time scale. We also observe that onset over CI occurs after the arrival of a westward propagating convective cell from the western Pacific in the Fav case. The spatial structures of the HF-ISO-filtered streamfunction anomalies reveal propagation of a double cell structure from the western Pacific: one along the CI latitudes and the other just to the south of the equator. The vertical structures of these cells are similar to the 10- to 20-day mode presented in Chen and Chen (1993), with the northern cell being more intense than the southern one. The arrival of the ascending limbs of both the ISO modes during onset in the Fav case possibly significantly enhances the amount of rainfall on that day over CI. On the contrary, when onset over CI occurs when both the ISO modes are not favorable (Nfav case), LF-ISO- or HF-ISO-filtered anomalies are weaker or show no signal of propagation, Hadley cell circulation shows weaker signal with Tibetan anticyclone not being established, skin temperature anomalies are much weaker, with weaker low-level winds. Furthermore, the atmosphere is comparatively more stable in the Nfav case than in the Fav case over CI during onset. We found that only 14 out of the 58 onset cases over CI are not influenced by the ISO modes (Nfav case). This suggests that onset over CI is modulated by the large-scale flow patterns associated with ISOs in majority of the cases. But we do not address what could have triggered the onset of the ISM in the Nfav cases, which is beyond the scope of this study. We speculate small-scale synoptic features may have a larger role to play in these cases and can be better addressed using a high-resolution climate model.

This study also demonstrates a possibility to predict local onset and demise of the ISM with the information of ISO phases. It is inferred that real-time forecasts of ISO phases and a better knowledge about the space-time structure of LF-ISO and HF-ISO could be used to perform superior probabilistic estimation of onset/demise of the ISM at local scale. This might have practical applications and significant implications to the agroeconomic society of India. Also, if we can improve the basic structures of the ISO modes in the numerical models, prediction of onset and demise of the ISM from such models can be enhanced. Although there are many studies addressing the structure of LF-ISO in state-of-the-art models (Sabeerali et al., 2013), there are very few studies that analyze the HF-ISO modes in models. However, present-day numerical models still suffer in producing accurate spatiotemporal structure of ISO.

Acknowledgments
We thank the anonymous reviewers for their constructive comments that helped us to significantly improve the quality of the manuscript. This work was funded by NASA grants NNX17AG72G and NNX16AD83G, NSF award 1606296, and the Earth System Science Organization, Ministry of Earth Sciences, Government of India (MM/SERP/FSU/2014/SSC-02/002). Data sets used in this study are from cited references.

References

Allen, M., & Robertson, A. (1996). Distinguishing modulated oscillations from coloured noise in multivariate datasets. *Climate Dynamics*, *12*(11), 775–784. https://doi.org/10.1007/s003820050142

Ananthakrishnan, R., Acharya, U., & Ramakrishnan, A. (1967). On the criteria for declaring the onset of the southwest monsoon over Kerala. *Forecasting Manual. FMU Report No. IV-18.1*, *52*, 1620–1639.

Bhatt, B. C., & Nakamura, K. (2005). Characteristics of monsoon rainfall around the Himalayas revealed by TRMM precipitation radar. *Monthly Weather Review*, *133*(1), 149–165. https://doi.org/10.1175/MWR-2846.1

Bombardi, R. J., Pegion, K. V., Kinter, J. L., Cash, B. A., & Adams, J. M. (2017). Sub-seasonal predictability of the onset and demise of the rainy season over monsoonal regions. *Frontiers of Earth Science*, *5*, 14. https://doi.org/10.3389/feart.2017.00014

Chakraborty, A., Nanjundiah, R. S., & Srinivasan, J. (2006). Theoretical aspects of the onset of Indian summer monsoon from perturbed orography simulations in a GCM. *Annales Geophysicae*, *24*(8), 2075–2089.

Chatterjee, P., & Goswami, B. N. (2004a). Structure, genesis and scale selection of the tropical quasi-biweekly mode. *Quarterly Journal of the Royal Meteorological Society*, *130*(599), 1171–1194. https://doi.org/10.1256/qj.03.133

Chatterjee, P., & Goswami, B. N. (2004b). Structure, genesis and scale selection of the tropical quasi-biweekly mode. *Quarterly Journal of the Royal Meteorological Society*, *130*(599), 1171–1194. https://doi.org/10.1256/qj.03.133

Chen, T.-C., & Chen, J.-M. (1993). The 10-20-day mode of the 1979 Indian monsoon: Its relation with the time variation of monsoon rainfall. *Monthly Weather Review*, *121*(9), 2465–2482. https://doi.org/10.1175/1520-0493(1993)121<2465:TDMOTI>2.0.CO;2

Fasullo, J., & Webster, P. (2003). A hydrological definition of Indian monsoon onset and withdrawal. *Journal of Climate*, *16*(19), 3200–3211.

Gadgil, S. (2003). The Indian monsoon and its variability. *Annual Review of Earth and Planetary Sciences*, *31*(1), 429–467. https://doi.org/10.1146/annurev.earth.31.100901.141251

Gadgil, S., & Gadgil, S. (2006). The Indian monsoon, GDP and agriculture. *Economic and Political Weekly*, *41*, 4887–4895.

Ghil, M., Allen, M., Dettinger, M., Ide, K., Kondrashov, D., Mann, M., et al. (2002). Advanced spectral methods for climatic time series. *Reviews of Geophysics*, *40*(1), 1003. https://doi.org/10.1029/2000RG000092

Giné, X., Townsend, R. M., & Vickery, J. (2008). Rational expectations? Evidence from planting decisions in semi-arid India (*Working paper No. 166*). Washington, DC: World Bank.

Goswami, B. N., & Ajaya Mohan, R. (2001). Intraseasonal oscillations and interannual variability of the Indian summer monsoon. *Journal of Climate*, *14*(6), 1180–1198. https://doi.org/10.1175/1520-0442(2001)014<1180:IOAIVO>2.0.CO;2

Goswami, B. N., Ajayamohan, R. S., Xavier, P. K., & Sengupta, D. (2003). Clustering of synoptic activity by indian summer monsoon intraseasonal oscillations. *Geophysical Research Letters*, *30*(8), 1431. https://doi.org/10.1029/2002GL016734

Goswami, B. N., & Xavier, P. K. (2005). ENSO control on the south Asian monsoon through the length of the rainy season. *Geophysical Research Letters*, *32*, L18717. https://doi.org/10.1029/2005GL023216

Hendon, H. H., & Salby, M. L. (1994). The life cycle of the Madden–Julian oscillation. *Journal of the Atmospheric Sciences*, *51*(15), 2225–2237.

Jiang, X., Li, T., & Wang, B. (2004). Structures and mechanisms of the northward propagating boreal summer intraseasonal oscillation. *Journal of Climate*, *17*(5), 1022–1039. https://doi.org/10.1175/1520-0442(2004)017<1022:SAMOTN>2.0.CO;2

Joseph, P. V., Eischeid, J. K., & Pyle, R. J. (1994). Interannual variability of the onset of the Indian summer monsoon and its association with atmospheric features, El Nino, and sea surface temperature anomalies. *Journal of Climate*, *7*(1), 81–105.

Joseph, P. V., Sooraj, K. P., & Rajan, C. K. (2006). The summer monsoon onset process over South Asia and an objective method for the date of monsoon onset over Kerala. *International Journal of Climatology*, *26*(13), 1871–1893.

Kalnay, E., Kanamitsu, M., Kistler, R., Collins, W., Deaven, D., Gandin, L., et al. (1996). The NCEP/NCAR 40-year reanalysis project. *Bulletin of the American Meteorological Society*, *77*(3), 437–471.

Karmakar, N., Chakraborty, A., & Nanjundiah, R. S. (2015). Decreasing intensity of monsoon low-frequency intraseasonal variability over India. *Environmental Research Letters*, *10*(5), 054018. https://doi.org/10.1088/1748-9326/10/5/054018

Karmakar, N., Chakraborty, A., & Nanjundiah, R. S. (2017a). Increased sporadic extremes decrease the intraseasonal variability in the Indian summer monsoon. *Scientific Reports*, *7*, 7824. https://doi.org/10.1038/s41598-017-07529-6

Karmakar, N., Chakraborty, A., & Nanjundiah, R. S. (2017b). Space-time evolution of the low- and high-frequency intraseasonal modes of the Indian summer monsoon. *Monthly Weather Review*, *145*(2), 413–435. https://doi.org/10.1175/MWR-D-16-0075.1

Karmakar, N., & Krishnamurti, T. N. (2018). Characteristics of northward propagating intraseasonal oscillation in the Indian summer monsoon. *Climate Dynamics*, 1–14. https://doi.org/10.1007/s00382-018-4268-2

Kemball-Cook, S., & Wang, B. (2001). Equatorial waves and air-sea interaction in the boreal summer intraseasonal oscillation. *Journal of Climate*, *14*(13), 2923–2942. https://doi.org/10.1175/1520-0442(2001)014

Klingaman, N. P., Weller, H., Slingo, J. M., & Inness, P. M. (2008). The intraseasonal variability of the Indian summer monsoon using TMI sea surface temperatures and ECMWF reanalysis. *Journal of Climate*, *21*(11), 2519–2539.

Krishnamurthy, V., & Shukla, J. (2007). Intraseasonal and seasonally persisting patterns of Indian monsoon rainfall. *Journal of Climate*, *20*(1), 3–20. https://doi.org/10.1175/JCLI3981.1

Krishnamurti, T., & Ardanuy, P. (1980). The 10 to 20-day westward propagating mode and Breaks in the Monsoons. *Tellus*, *32*(1), 15–26. https://doi.org/10.1111/j.2153-3490.1980.tb01717.x

Krishnamurti, T. N., & Bhalme, H. (1976). Oscillations of a monsoon system. Part I. Observational aspects. *Journal of the Atmospheric Sciences*, *33*(10), 1937–1954. https://doi.org/10.1175/1520-0469(1976)033<1937:OOAMSP>2.0.CO;2

Krishnamurti, T. N., Jayakumar, P., Sheng, J., Surgi, N., & Kumar, A. (1985). Divergent circulations on the 30 to 50 day time scale. *Journal of the Atmospheric Sciences*, *42*(4), 364–375. https://doi.org/10.1175/1520-0469(1985)042<0364:DCOTTD>2.0.CO;2

Krishnamurti, T. N., & Ramanathan, Y. (1982). Sensitivity of the monsoon onset to differential heating. *Journal of the Atmospheric Sciences*, *39*(6), 1290–1306.

Krishnamurti, T. N., Simon, A., Thomas, A., Mishra, A., Sikka, D., Niyogi, D., et al. (2012). Modeling of forecast sensitivity on the march of monsoon isochrones from Kerala to New Delhi: The first 25 days, *69*(8), 2465–2487.

Lee, J.-Y., Wang, B., Wheeler, M. C., Fu, X., Waliser, D. E., & Kang, I.-S. (2013). Real-time multivariate indices for the boreal summer intraseasonal oscillation over the Asian summer monsoon region. *Climate Dynamics*, *1-2*, 493–509.

Levine, R. C., Turner, A. G., Marathayil, D., & Martin, G. M. (2013). The role of northern Arabian Sea surface temperature biases in CMIP5 model simulations and future projections of Indian summer monsoon rainfall. *Climate Dynamics*, *41*(1), 155–172.

Liebmann, B., & Marengo, J. (2001). Interannual variability of the rainy season and rainfall in the Brazilian Amazon Basin. *Journal of Climate*, *14*(22), 4308–4318.

Mani, M., Bandyopadhyay, S., Chonabayashi, S., Markandya, A., & Mosier, T. (2018). South Asia's hotspots: The impact of temperature and precipitation changes on living standards, *South Asia Development Matters*. Washington, DC: The World Bank. https://openknowledge.worldbank.org/handle/10986/28723

Misra, V., Bhardwaj, A., & Mishra, A. (2017). Local onset and demise of the indian summer monsoon. *Climate Dynamics*, *51*, 1609–1622. https://doi.org/10.1007/s00382-017-3924-2

Misra, V., Bhardwaj, A., & Noska, R. (2017). Understanding the variations of the length and the seasonal rainfall anomalies of the Indian summer monsoon. *Journal of Climate*, *30*(5), 1753–1763.

Moron, V., & Robertson, A. W. (2014). Interannual variability of Indian summer monsoon rainfall onset date at local scale. *International Journal of Climatology*, *34*(4), 1050–1061.

Moron, V., Robertson, A., & Ghil, M. (2012). Impact of the modulated annual cycle and intraseasonal oscillation on daily-to-interannual rainfall variability across monsoonal India. *Climate Dynamics*, *38*(11-12), 2409–2435. https://doi.org/10.1007/s00382-011-1253-4

Moron, V., Robertson, A. W., & Pai, D. (2017). On the spatial coherence of sub-seasonal to seasonal Indian rainfall anomalies. *Climate Dynamics*, *49*(9-10), 3403–3423.

Murakami, M. (1976). Analysis of summer monsoon fluctuations over India. *Journal of the Meteorological Society of Japan*, *54*(1), 15–31.

Neelin, J. D., & Held, I. M. (1987). Modeling tropical convergence based on the moist static energy budget. *Monthly Weather Review*, *115*(1), 3–12.

Noska, R., & Misra, V. (2016). Characterizing the onset and demise of the Indian summer monsoon. *Geophysical Research Letters*, *43*, 4547–4554. https://doi.org/10.1002/2016GL068409

Pai, D. S., & Bhan, S. C. (2014). Monsoon 2013: A report (IMD Met. Monograph No: ESSO/IMD/SYNOPTIC MET/01-2014/15). Pune, India: India Meteorological Department, National Climate Center.

Pai, D. S., & Bhan, S. C. (2015). Monsoon 2014: A report (IMD Met. Monograph No: ESSO/IMD/SYNOPTIC MET/01(2015)/17). Pune, India: India Meteorological Department, National Climate Center.

Pai, D. S., & Rajeevan, M. (2009). Summer monsoon onset over Kerala: New definition and prediction. *Journal of Earth System Science*, *118*(2), 123–135.

Pai, D. S., Sridhar, L., Rajeevan, M., Sreejith, O., Satbhai, N., & Mukhopadhyay, B. (2014). Development of a new high spatial resolution (0.25×0.25) long period (1901–2010) daily gridded rainfall data set over India and its comparison with existing data sets over the region. *Mausam*, *65*(1), 1–18.

Parker, D. J., Willetts, P., Birch, C., Turner, A. G., Marsham, J. H., Taylor, C. M., & Martin, G. M. (2016). The interaction of moist convection and mid-level dry air in the advance of the onset of the Indian monsoon. *Quarterly Journal of the Royal Meteorological Society*, *142*(699), 2256–2272.

Plaut, G., & Vautard, R. (1994). Spells of low-frequency oscillations and weather regimes in the Northern Hemisphere. *Journal of the Atmospheric Sciences*, *51*(2), 210–236. https://doi.org/10.1175/1520-0469(1994)051

Rajeevan, M., Gadgil, S., & Bhate, J. (2010). Active and break spells of the Indian summer monsoon. *Journal of the Atmospheric Sciences*, *119*(3), 229–247. https://doi.org/10.1007/s12040-010-0019-4

Rajeevan, M., Unnikrishnan, C., Bhate, J., Niranjan Kumar, K., & Sreekala, P. (2012). Northeast monsoon over India: Variability and prediction. *Meteorological Applications*, *19*(2), 226–236.

Sabeerali, C., Ramu Dandi, A., Dhakate, A., Salunke, K., Mahapatra, S., & Rao, S. A. (2013). Simulation of boreal summer intraseasonal oscillations in the latest CMIP5 coupled GCMs. *Journal of Geophysical Research: Atmospheres*, *118*, 4401–4420. https://doi.org/10.1002/jgrd.50403

Sabeerali, C., Rao, S. A., Ajayamohan, R., & Murtugudde, R. (2012). On the relationship between Indian summer monsoon withdrawal and Indo-Pacific SST anomalies before and after 1976/1977 climate shift. *Climate Dynamics*, *39*(3-4), 841–859.

Schiemann, R., Lthi, D., & Schr, C. (2009). Seasonality and interannual variability of the westerly jet in the Tibetan Plateau region. *Journal of Climate*, *22*(11), 2940–2957. https://doi.org/10.1175/2008JCLI2625.1

Sengupta, D., Goswami, B., & Senan, R. (2001). Coherent intraseasonal oscillations of ocean and atmosphere during the Asian summer monsoon. *Geophysical Research Letters*, *28*(21), 4127–4130.

Sikka, D., & Gadgil, S. (1980). On the maximum cloud zone and the ITCZ over Indian, longitudes during the southwest monsoon. *Monthly Weather Review*, *108*(11), 1840–1853. https://doi.org/10.1175/1520-0493(1980)108<1840:OTMCZA>2.0.CO;2

Sperber, K. R., & Annamalai, H. (2014). The use of fractional accumulated precipitation for the evaluation of the annual cycle of monsoons. *Climate Dynamics*, *12*, 3219–3244.

Srinivasan, J., & Smith, G. (1996). The role of heat fluxes and moist static energy in tropical convergence zones. *Monthly Weather Review*, *10*, 2089–2099.

Syroka, J., & Toumi, R. (2002). Recent lengthening of the south Asian summer monsoon season. *Geophysical Research Letters*, *29*(10), 1458. https://doi.org/10.1029/2002GL015053

Wang, B., Ding, Q., & Joseph, P. V. (2009). Objective definition of the Indian summer monsoon onset. *Journal of Climate*, *22*(12), 3303–3316.

Wang, B., & LinHo (2002). Rainy season of the Asian-Pacific summer monsoon. *Journal of Climate*, *15*(4), 386–398. https://doi.org/10.1175/1520-0442(2002)015<0386:RSOTAP>2.0.CO;2

Webster, P. J., Magaña, V. O., Palmer, T. N., Shukla, J., Tomas, R. A., Yanai, M., & Yasunari, T. (1998). Monsoons: Processes, predictability, and the prospects for prediction. *Journal of Geophysical Research*, *103*(C7), 14,451–14,510. https://doi.org/10.1029/97JC02719

Webster, P. J., & Yang, S. (1992). Monsoon and ENSO: Selectively interactive systems. *Quarterly Journal of the Royal Meteorological Society*, *118*(507), 877–926.

Wu, M. L. C., Schubert, S., & Huang, N. E. (1999). The development of the South Asian summer monsoon and the intraseasonal oscillation. *Journal of Climate*, *12*(1), 2054–2075.

Xavier, P. K., Marzin, C., & Goswami, B. (2007). An objective definition of the Indian summer monsoon season and a new perspective on the ENSO–monsoon relationship. *Quarterly Journal of the Royal Meteorological Society*, *133*(624), 749–764.

Yanai, M., Li, C., & Song, Z. (1992). Seasonal heating of the Tibetan Plateau and its effects on the evolution of the Asian summer monsoon. *Journal of the Meteorological Society of Japan Series II*, *70*(1B), 319–351.

Yasunari, T. (1980). A quasi-stationary appearance of 30 to 40 day period in the cloudiness fluctuations during the summer monsoon over India. *Journal of the Meteorological Society of Japan*, *58*, 225–229.

Zhou, L., & Murtugudde, R. (2014). Impact of northward-propagating intraseasonal variability on the onset of Indian summer monsoon. *Journal of Climate*, *27*(1), 126–139.